Enzymatic Activity of Individual Bioelectrocatalytic Viral Nanoparticles: Dependence of Catalysis on the Viral Scaffold and its Length

Telmo O Paiva, Angela N Schneider, Laure Bataille, Arnaud Chovin, Agnès Anne, Thierry Michon, Christina Wege, Christophe Demaille

Nanoscale

Accepted Manuscript

This article can be cited before page numbers have been issued, to do this please use: T. Oliveira Paiva, A. N. Schneider, L. Bataille, A. Chovin, A. Anne, T. Michon, C. Wege and C. Demaille, *Nanoscale*, 2022, DOI: 10.1039/D1NR07445H.

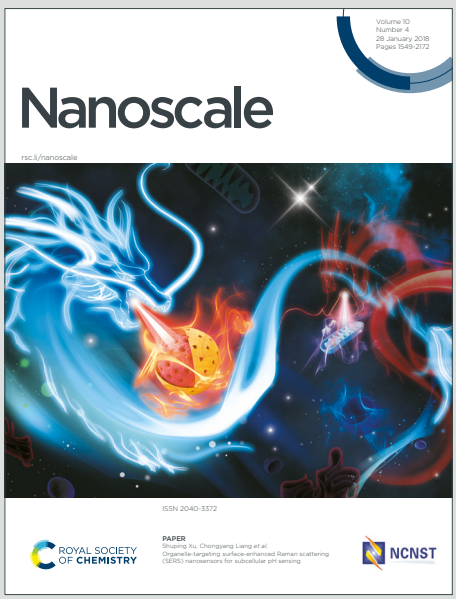

ROYAL SOCIETY OF CHEMISTRY

rsc.li/nanoscale

View Article Online
DOI: 10.1039/D1NR07445H

ARTICLE

Enzymatic Activity of Individual Bioelectrocatalytic Viral Nanoparticles: Dependence of Catalysis on the Viral Scaffold and its Length

Received 00th January 20xx,
Accepted 00th January 20xx

DOI: 10.1039/x0xx00000x

Telmo O. Paiva,[a] Angela Schneider,[b] Laure Bataille,[c] Arnaud Chovin,[a] Agnès Anne,[a] Thierry Michon,*[c] Christina Wege,*[b] Christophe Demaille *[a]

The enzymatic activity of tobacco mosaic virus (TMV) nanorod particles decorated with an integrated electro-catalytic system, comprising the quinoprotein glucose-dehydrogenase (PQQ-GDH) enzyme and ferrocenylated PEG chains as redox mediators, is probed at the individual virion scale by scanning electrochemical atomic force microscopy (AFM-SECM). A marked dependence of the catalytic activity on the particle length is observed. This finding can be explained by electron propagation along the viral backbone, resulting from electron exchange between ferrocene moieties, coupled with enzymatic catalysis. Thus, the use of a simple 1D diffusion/reaction model allows the determination of the kinetic parameters of the virus-supported enzyme. Comparative analysis of the catalytic behavior of the Fc-PEG/PQQ-GDH system assembled on two differing viral scaffolds, TMV (this work) and bacteriophage-*fd* (previous work), reveals two distinct kinetic effects of scaffolding: An enhancement of catalysis that does not depend on the virus type and a modulation of substrate inhibition that depends on the virus type. AFM-SECM detection of the enzymatic activity of a few tens of PQQ-GDH molecules, decorating a 40 nm-long viral domain, is also demonstrated, a record in terms of the lowest number of enzyme molecules interrogated by an electrochemical imaging technique.

1. Introduction

Deciphering the mechanism of catalytic enhancement resulting from the immobilization of enzyme molecules onto nanometer-sized scaffolds is a very active research topic, and is key to engineer higher performance bioreactors, biosensors or biofuel cells.[1–3] Catalytic enhancement has been extensively documented for systems comprising a *single type* of enzyme and demonstrated for a wide range of enzymatic reactions and scaffold types.[4,5] Amongst them are bionanoscaffolds, such as DNA nanostructures,[6,7] including DNA origamis,[8] or harmless viral particles (virions) from plants, as well as bacteriophages.[9,10] In the two latter cases, of particular interest here, enzymes have been either displayed on the surface of the particles (capsid),[11–20] or confined in empty virus-like particles (VLPs).[21–26] *Multi*-enzyme systems, where differing enzymes work in cascade, have also been assembled on DNA origamis[27,28] and viral particles.[29–35] In many instances, these artificial enzymatic cascades showed better activity than the cascaded enzymes freely cooperating in solution.[36–39] This improvement was initially assigned to a more efficient channeling of the metabolites between the immobilized cascade enzymes.[40,41] However, it has recently been pointed out that an enhancement of the catalytic performances of the *individual* enzymes in such cascades, rather than channeling, may account for the superior activity of scaffolded multienzymatic systems.[42–44] The question of the role played by the scaffold material itself in modulating enzyme activity thus arose, and it was suggested that the specific microenvironment provided by nanoscaffolds could modify enzyme reaction kinetics.[44,45] Two main mechanisms have been proposed so far to explain, at least partially, this microenvironment effect.

The first is related to the highly charged nature of bioscaffolds. It has, for example, been evidenced that the highly negatively charged surface of DNA scaffolds can make the local pH more acidic than that of the solution, bringing it closer to the optimal pH of the attached enzymes.[44,46] A similar charge-related pH change has also been observed inside VLPs used to confine enzyme molecules.[47] In addition, the flux of substrates toward virion-encapsulated enzymes was also shown to be controlled by the electric charge present around the pores of the viral capsid.[23]

The second proposed mechanism relies on the establishment of transient binding interactions between the enzymatic *substrate molecules* and the scaffold, as originally identified for DNA-scaffolded, or simply DNA-decorated, enzymes.[48–50] In these cases, DNA-substrate interactions have been shown to result in an increased apparent affinity of the enzymes for their substrate, due to higher substrate molarity in

[a] Université de Paris, Laboratoire d'Electrochimie Moléculaire, CNRS UMR 7591, F-75013 Paris, France. E-mail: christophe.demaille@u-paris.fr
[b] University of Stuttgart, Institute of Biomaterials and Biomolecular Systems, Research Unit Molecular and Synthetic Plant Virology, 70569 Stuttgart, Germany. E-mail: christina.wege@bio.uni-stuttgart.de
[c] Université de Bordeaux, Biologie du Fruit et Pathologie, INRA UMR 1332, F-33140 Villenave d'Ornon, France. E-mail: thierry.michon@inrae.fr
† Electronic Supplementary Information (ESI) available. See DOI: 10.1039/x0xx00000x

the enzymes' vicinity. Likewise, binding of inhibitors to DNA resulted in increased apparent enzyme inhibition.[49]

Overall, although the mechanisms responsible for nano-scaffolding-induced catalytic enhancement have not yet all been identified, the role played by the scaffold itself appears to be decisive and needs to be studied further.[45] One way to address this issue is to assemble the *same* enzymatic system on scaffolds incrementally differing in their dimensions and/or physico-chemical properties, and monitor the resulting changes in the kinetic behavior of the enzyme. This is what is attempted here, by use of a catalytic system consisting of a single enzyme type and its tethered co-substrate.

In a previous paper, we immuno-assembled an integrated glucose-oxidizing enzymatic system, consisting of the enzyme quinoprotein glucose dehydrogenase (PQQ-GDH) and polyethyleneglycol-borne ferrocene moieties (Fc-PEG) as its redox cobsubstrate, onto filamentous *fd*-bacteriophage particles adsorbed on electrode surfaces.[51] We showed that confinement of the integrated enzymatic system on the viral scaffolds endowed the *fd*-supported integrated enzymatic system with optimal catalytic performance. Subsequently atomic force-electrochemical microscopy (AFM-SECM),[52,53] implemented in a redox mediator-tethered (Mt) mode,[54] was used to quantify the enzymatic activity of *individual* decorated *fd* particles adsorbed onto insulating surfaces.[55] Herein, we have conducted a single particle Mt/AFM-SECM investigation of the same Fc-PEG/PQQ-GDH integrated system, but assembled on another type of viral scaffold, namely tobacco mosaic virus (TMV),[56] primarily differing from *fd* by its shorter length and lower electric surface charge. This enables us to shed light on the relation between the physical properties of viral nanoscaffolds and the catalytic activity of the enzymatic system they bear.

Finally, our immuno-assembly approach has been used to selectively decorate short (40 nm) terminal domains of composite TMV-like particles (TLPs) with two differentially addressable longitudinal subdomains ('domain-TLPs', DTLPs). Mt/AFM-SECM probing of the catalytic activity of such nano-domain, bearing ~ 10 enzymes molecules in total, is demonstrated, setting a new record in SECM studies of enzymatic catalysis.[57–60]

2. Experimental Section

2.1. Biological material

Virus Particles. The tobacco mosaic virus mutant TMV_{Cys} was generated *in vitro* by genetic modification of TMV to expose thiol groups close to the N-terminus of every CP (mutant S3C) on its outer surface, as described earlier.[61] Two domain-TMV-like particles (DTLPs), namely CP_{Cys}/$CP_{Cys\text{-}bio}$-DTLPs were composed of two domains of N-terminally (with regard to the RNA template's orientation) cysteine-modified coat proteins (CP_{Cys}, 260 nm), and 3'-terminally cysteine-modified CPs covalently functionalized by biotin moieties prior to their *in vitro* assembly ($CP_{Cys\text{-}bio}$, 40 nm). These DTLPs were assembled *in vitro*, using a dynamic DNA technology-based approach to control their stepwise growth from the two types of TMV CP subunits and RNA, adapted from Schneider et al.[62] For that purpose, 240 nmol of a DNA oligonucleotide strand (stopper) was hybridized to 20 µg (9.6 pmol) TMV RNA (corresponding to a 25-fold molar excess of stopper over the RNA) at 30 °C for 2 h. Subsequently, the RNA's encapsidation into a a CP helix was initiated by the addition of 400 µg CP_{Cys} and achieved by incubation at 25 °C for 3 h, to generate partially assembled tubes blocked site-specifically at the DNA/RNA hybrid position. To remove non-assembled RNA and CP molecules, the desired product was sedimented *via* ultracentrifugation (UC) in a 45 Ti rotor Optima L90K (Beckman Coulter GmbH, Krefeld, Germany) at 119 000 *g*, 4 °C, for 2 h. The pellet was dissolved in 75 mM sodium potassium phosphate buffer (SPP, pH 7.4) and incubated at 25 °C for 5 h with 150 µg $CP_{Cys\text{-}bio}$ (3-fold assembly excess over the remaining RNA-tail) and 100 pmol of a release strand, fully complementary to the stopper (corresponding to a 10-fold molar excess over bound stopper), to reinitiate the assembly of the second $CP_{Cys\text{-}bio}$ domain. To purify and concentrate the CP_{Cys}/$CP_{Cys\text{-}bio}$-DTLPs, a final UC step was applied at 119 000 g, 4 °C, for 2 h and the pellet resuspended and stored in 10 mM SPP, pH 7.4.

Antibodies. The anti-TMV polyclonal rabbit IgG antibody (purified IgG fraction) was provided by K.W. Mundry and E. Hornung, previously University of Stuttgart (Germany). The anti-biotin polyclonal rabbit secondary IgG antibody was obtained from Bethyl Laboratories (USA). The goat anti-rabbit IgG secondary antibody, to be conjugated with GDH or Fc-PEG chains, was from Jackson ImmunoResearch Laboratories (UK). The anti-GDH polyclonal antibody was custom-produced in rabbit by Genosphere Biotechnologies using apo-GDH monomers as antigens. All antibody solutions contained 1 mg/ml BSA and 0.01 % (w:v) sodium azide (NaN3) preservative.

Enzymes. The holo-GDH (PQQ-GDH) was produced and reconstituted from apo-GDH (from Escherichia coli strain BL21(DE3) transformed with plasmid pgp492) as detailed previously,[51] and used to prepare the anti-rabbit PQQ-GDH-IgG conjugate as described earlier.[51] Apo-GDH (GD-2) employed for spectrophotometric assays of PQQ was from Sekisui enzymes.

2.2. Chemicals and solutions.

The bovine serum albumin (BSA) (IgG-free grade) blocking agent, was from Jackson ImunoResearch Laboratories (UK). 11-aminoundecyltriethoxysilane (AUTES) and phenazine methosulphate (PMS) were obtained from Alfa Aesar. 2,6-dichlorophenolindophenol (DCPIP), and all other analytical grade chemicals were Sigma-Aldrich products and used as received. All solutions were prepared with double-deionized water (18.2 MΩ cm^{-1} resistivity, TKA Micro-Pure UV). Two buffer solutions were used for surface assembly: 10 mM sodium-potassium phosphate (SPP) buffer at pH 7.4 (phosphate buffer), and 50 mM Tris-HCl buffer at pH 7.5 (Tris buffer). SPP buffer was used for the preparation of the viruses, anti-viruses and anti-biotin antibody solutions. Tris-HCl buffer was used to prepare the solutions of all the other antibodies, and also as the imaging medium for the *in situ* AFM-SECM experiments. The stock

solutions of glucose in Tris-HCl buffer were allowed to mutarotate overnight.

2.3. Preparation and characterization of IgG-PEG-Fc redox antibody

The IgG-PEG-Fc redox antibody was prepared by covalent conjugation of the Fc-PEG chains to the goat anti-rabbit IgG, by reacting the NHS-activated ester of a home-synthesized NHS-PEG3500-Fc chain[63] with the amino groups of lysine residues exposed on the IgG surface. The redox PEGylation procedure has been described in detail previously.[51]

2.4. Assembly of the virus-scaffolded integrated redox enzymatic system on SiO_2 surfaces

Ultra-flat SiO_2 chips. Ultra-flat silicon dioxide substrates (SiO_2 chips), from NanoAndMore, were used to support the virus-scaffolded integrated systems. They consisted of a 200 nm-thick amorphous SiO_2 layer thermally grown on a 5 x 5 mm^2 ultra-flat silicon chip.

Amino-C_{11} modified ultra-flat SiO_2 surfaces. The ultra-flat SiO_2 chip was UV-ozone cleaned for 5 min, rinsed with water and ethanol, and immersed in a 1 mM 11-aminoundecyl triethoxysilane (AUTES) solution in ethanol for 30 min. The thus-obtained amino-C_{11}-silane modified chip was rinsed again with ethanol, then water and annealed at 120 °C for 45 min. The chip was glued on a 2 x 2 cm^2 glass slide with double-sided tape and masked with a perforated Teflon adhesive mask, to form a 4 mm diameter disk-shaped amino-C_{11} modified ultra-flat SiO_2 surface.

Random TMV_{Cys} or DTLP virus arrays on SiO_2 surfaces. To promote the formation of the TMV_{Cys} or DTLP arrays, the amino-C_{11}-silane SiO_2 surface was left in contact with a 20 µL drop of SPP buffer solution containing 1.0 µg/mL of TMV_{Cys} or DTLPs, respectively, during 15 min. Two droplet replacement steps and a 10 min desorption step in phosphate buffer were then carefully performed. In order to reinforce adhesion of the virus particles, the surface was gently dried under a N_2 flux and rehydrated afterwards with SPP buffer. A surface coverage of ~1.0 TMV_{Cys} particles per μm^2 was achieved. For the adsorption of the CP_{Cys}/$CP_{Cys\text{-}bio}$ DTLPs, a 3 µg/mL virus solution was used, yielding a surface concentration of ~3 DTLPs per μm^2.

Protective BSA backfilling. The virus arrayed-surface was then exposed to 20 µL of 2.0 mg/mL BSA in SPP buffer solution for 1 h, to block non-specific binding during the immuno-assembly steps. This was followed by two subsequent rinsing and 10 min desorption steps with SPP buffer.

Assembly of the anti-TMV or anti-biotin antibody. The BSA-backfilled surface was incubated with 20 µL of 2 µg/mL (~0.80 10^{13} molecules/mL) anti-TMV, or anti-biotin, respectively, rabbit antibody solution for 1 h, followed by two droplet replacement rinsing and desorption steps of 10 min each. The TMV/DTLP-equipped and pre-functionalized SiO_2 chips were stored overnight, in SPP buffer solution containing 1 mg/mL BSA and 0.01 % (w:v) sodium azide, at room temperature and protected from light.

Assembly of the PQQ-GDH conjugated antibody. The surface was left in contact for 2 h with a 5 µg/mL (~1.2 10^{13} molecules/mL) anti-rabbit GDH-IgG conjugate solution in Tris-HCl buffer. Two 5 min rinsing/desorption steps were then performed with Tris-HCl buffer containing 1 mg/mL BSA.

Assembly of the anti-GDH antibody. The surface was exposed to 20 µL of a 5 µg/mL solution of rabbit anti-GDH IgG in Tris-HCl buffer for 1 h. After rinsing by drop replacement and two 5 min desorption steps, the surface was left to desorb for 10 min in Tris-HCl buffer containing 1 mg/mL BSA.

Assembly of the IgG-PEG-Fc antibody. 20 µL of the 20 µg/mL anti-rabbit IgG-PEG-Fc solution in Tris-HCl buffer were then deposited on the surface, and left to incubate overnight at 4°C under a water-saturated atmosphere and protected from light. Two rinsing/desorption steps of 5 min each were then carried out using Tris-HCl buffer solution containing 1 mg/mL BSA.

2.5. Quantification by cyclic voltammetry of the number of ferrocene units decorating the TMV particles assembled on ultraflat gold surfaces – See ESI

2.6. Assaying the number of PQQ-GDH molecules decorating the TMV particles by spectrophotometry – See ESI

2.7. AFM and AFM-SECM imaging

AFM imaging. Tapping mode AFM images were acquired with a Nanowizard II microscope (JPK, Germany). *In situ* imaging (in phosphate or Tris buffer) was carried out with home-made gold tips prepared from 25 µm diameter etched and flattened gold wires. These tips were ~40 times softer than those we described previously, which were prepared from 60 µm diameter gold wires.[64] These new soft probes are characterized by a spring constant in the order of 0.1 nN/nm, a flexural frequency of ~ 0.5-1 kHz and a typical tip radius of ~50 nm (see ESI). In our hands, they proved to be much less prone to contamination than equivalent commercial tips when imaging viral particles.

AFM-SECM imaging. Mt/AFM-SECM images were acquired using the JPK Nanowizard II microscope operated in AFM-SECM mode as previously described.[63] AFM-SECM tips were the same hand-fabricated gold tips used for AFM imaging, which were insulated by deposition of an electrophoretic paint, as described previously.[64] For consistency, the data reported were acquired with a limited set of tips, having similar radii of ~50 nm. The JPK electrochemical liquid cell, containing 1 mL of Tris-HCl buffer, was equipped with a platinum wire counter-electrode, and a polypyrrole-coated platinum wire as a quasi-reference electrode. All potentials are reported *versus* the KCl-saturated calomel electrode (SCE) reference. An in-house fabricated, high-gain bipotentiostat was used to control the tip potential *versus* the reference electrode, and to measure the tip current. The tip current signal was passed through a 10 Hz low-pass analogue filter. Slow enough image scan rates (0.2-0.3 Hz) were used to avoid distortion of the current image by the filter. In order to vary the glucose concentration in the cell, the tip was withdrawn a few µm away from the surface and 100 µL of 10 mM to 1 M stock solutions of glucose were injected into the cell using a micro-syringe equipped with a long bent metallic needle. After injection, glucose concentration was homogenized by repeatedly pumping/re-injecting ~ 100 µL of

View Article Online DOI: 10.1039/D1NR07445H

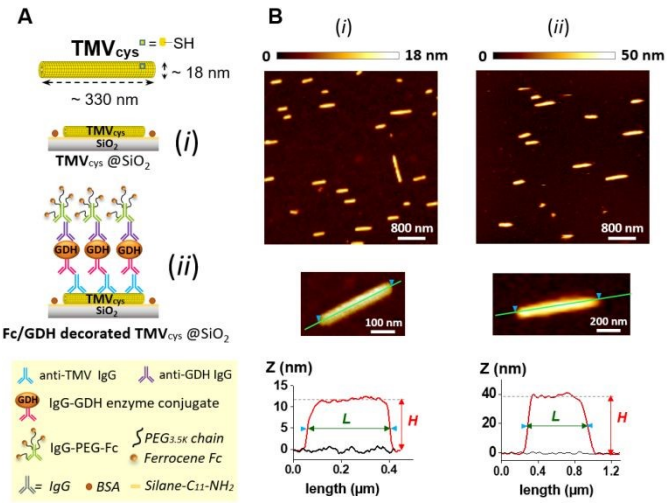

Fig. 1. (A) Schematic representation of a TMV_{Cys} virion adsorbed onto the SiO_2 surface as a bare particle, (*i*), and once decorated with the Fc-PEG/PQQ-GDH integrated system, (*ii*). **(B)** Tapping mode AFM images of an array of TMV virions, either bare, (*i*), or bearing the integrated system, (*ii*). The length, *L,* and height, *H*, of individual particles were measured from height profiles taken along their contour length, as shown. The images were acquired using AFM tips home-made from flattened 25 μm gold wires. Imaging buffer: Tris-HCl pH 7.5.

the cell solution using the micro-syringe. The tip was then brought back to the sample and the surface imaged again. The tapping mode imaging conditions were soft enough for the viral particles to be recursively imaged without being damaged by the tip. Little or no numerical post-filtering was applied to the images that were processed using the WSxM software.[65]

3. Results and Discussion

In the present work we made use of tobacco mosaic virus (TMV) particles as bionanoscaffolds to assemble an integrated Fc-PEG/PQQ-GDH enzymatic system. Wild type (*wt*) TMV has been heavily used in viral nanotechnology for decades[66] due to the fact that it is harmless to humans and can be produced easily with high yields. Its structure is perfectly characterized: it is composed of about 2130 capsid (or coat) proteins (CPs) assembled around its single-stranded ribonucleic acid (ssRNA) genome to form a rigid rod-shaped nucleoprotein helix, 300 nm in full length and 18 nm in diameter (Fig. 1A).[67] Its isoelectric point, pI ~ 3.5,[68] makes it a highly negatively charged particle at physiological pH.

Here, we considered a specific mutant of TMV, TMV_{Cys}, which is similar in size and in charge to *wt*-TMV,[61,69] but exposes cysteine side chains on every CP. The reason for this choice is that surface immobilization was found to be more efficient for this mutant, which has also been preferably used to display enzymes for biosensing applications.[16–18,30]

3.1 Formation of random nanoarrays of TMV_{Cys} on SiO_2 surfaces.

TMV_{Cys} nanoparticles were adsorbed onto SiO_2 surfaces bearing a positively charged, adhesion-promoting, C11-amino-silane self-assembled monolayer, from sodium potassium phosphate buffer pH 7.4. After adsorption, the surface was backfilled with bovine serum albumin (BSA), and imaged *in situ* by tapping mode AFM. Imaging was carried out with home-fabricated soft AFM probes, prepared from 25 μm diameter gold wires (see ESI).[64] A typical 5 μm x 5 μm topographic tapping mode AFM image of a SiO_2 surface bearing a random array of TMV_{Cys} particles is shown in Fig. 1B(i). The numerous elongated objects can be assigned to individual TMV_{Cys} virions. From such images, it is possible to measure the length, *L*, and height, *H*, of individual particles, as represented in the cross-section (height profile) of the zoomed-in image presented in Fig. 1B(i).

Acquiring numerous 5 μm x 5 μm tapping mode topographic images allowed us to measure *L* and *H* for several tens of individual particles and to build the corresponding histogram plots presented in Fig. 2A and Fig. 2B, respectively.

From these, three populations of TMV_{Cys} particles, differing by their length distribution, can be identified. Each of the populations, labeled 1, 2, 3, are characterized by an average length value, L_{av}, and a relative standard deviation value, *RSD, of* : $L_{av,1}$ = 190 nm, RSD_1 = 19%, $L_{av,2}$ = 330 nm, RSD_2 = 8.5%, $L_{av,3}$ = 670 nm, RSD_3 = 30%.

We estimate that a conservative value for the uncertainty on our length determination based on height profiles is ± 10 nm. Therefore, any absolute standard deviation in *L* value in excess of ~10 nm is indicative of an actual dispersion of the particles' length. In addition, tip convolution effects are likely to result in an overestimation of the particle length by ~10 nm.

Hence, it can be safely concluded that the central particle population characterized by $L_{av,2}$ = 330 nm, and by a narrow distribution, can be attributed to monomeric TMV virions. The population of shorter particles likely corresponds to breakage products, but also to incompletely assembled virions and virus-like particles with subgenomic or non-viral RNAs. The population of longer particles is composed of head-to-tail TMV dimers or oligomers, typically found in TMV preparations.[62]

The height histogram presented in Fig. 2B shows a unimodal distribution, characterized by an average height H_{av} = 11 nm and

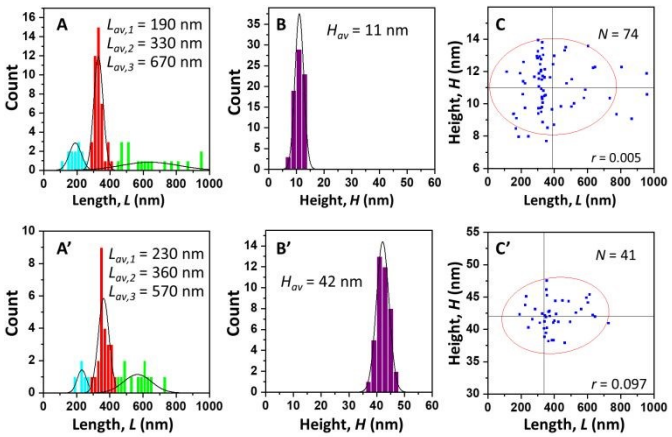

Fig. 2. Statistical distribution of the length, *L*, and height, *H*, of SiO_2-adsorbed TMV_{Cys} particles, either bare (A), (B), (C), or decorated with the Fc-PEG/PQQ-GDH system (A'), (B'), (C'). (A) and (A') are length histograms, (B) and (B') are height histograms. (C) and (C') are cross-correlation plots where the height of the particles is plotted versus their respective length. 95% confidence ellipses are drawn in (C) and (C'). *N* is the number of particles interrogated and *r* is the Pearson's correlation coefficient. L_{av} and H_{av} values are population averages. *H* and *L* were measured from tapping mode AFM imaging. Imaging buffer Tris-HCl pH 7.5

a 15% relative standard deviation. This is a first indication that

all TMV_{Cys} particles have similar height, no matter of their actual length. This result can be confirmed by constructing the cross-correlation graph shown in Fig. 2C, where the height of each particle is plotted as a function of its length. Random scattering of the data and the vanishingly small value obtained for the Pearson's correlation coefficient, r = 0.005, demonstrate the lack of correlation between the particles' height and length.

The average particle height, H_{av} = 11 nm, is close to, albeit smaller than, the diameter of TMV (18 nm). This can be partly explained by the fact that H is measured versus the BSA layer, whose thickness can amount for a few nanometers, considering the dimension of the BSA molecule (14 nm × 4 nm × 4 nm).[70] Besides, it is well known that AFM measurements tend to underestimate the height of biomolecules, due to their compression by the tip. Indeed, binding of TMV to inorganic surfaces was studied earlier and imaging heights from 10 to 18 nm were observed,[71] depending on virus-substrate interactions, in agreement with what was found here.

3.2. AFM-based monitoring of the decoration of TMV by the integrated system

Surface adsorbed TMV_{Cys} virions were decorated with the Fc-PEG/PQQ-GDH integrated system using the following immunological assembly process. The BSA-blocked SiO_2 surface bearing the viral random array was successively exposed to: (*i*) anti-TMV antibodies (Immunoglobulins G, IgG) produced in rabbit, (*ii*) a home-prepared GDH-anti-rabbit IgG conjugate, (*iii*) an anti-GDH rabbit IgG, (*iv*) a redox-functionalized anti-rabbit IgG, bearing covalently attached PEG_{3400} chains terminated by a ferrocene (Fc) head, the IgG-PEG-Fc.[72] Every step was separated by thorough rinsing with buffer. The antibody concentrations and exposure times were high enough for a full, saturating antibody layer to be assembled on the viral capsid at every step (see experimental section and AFM characterization below). The structure of the resulting fully decorated TMV is schematized in Fig. 1A(ii).

The assembly process was monitored by imaging the surface after each decoration step and measuring the particles' average height. The particle height was increased after each antibody immobilization step, indicating the effective assembly of a new antibody layer on the virion, Fig. S1. After immobilization of the last IgG type, the IgG-PEG-Fc, an average height value H_{av} = 42 nm was reached. This value is smaller than the expected approximate height of the decorated particle of ~ 60 nm, estimated from the height of the bare particle (11 nm) and counting a ~10 nm height increment per immobilized macromolecule (IgG or PQQ-GDH). This apparent discrepancy can be explained by the softness and overall flexibility of the multi-layered antibody assembly. As the number of antibody layers increases, the assembly likely becomes increasingly flexible and it is consequently less sensibly sensed by the AFM tip.

Careful analysis of numerous *in situ* tapping mode images of *fully-decorated* TMV allowed constructing the length and height histograms presented in Fig. 2A' and Fig. 2B', respectively. In Fig. 2A' one recognizes the three distinct populations of particles identified before decoration. After decoration, they are characterized by: $L_{av,1}$ = 230 nm, RSD_1 = 12%, $L_{av,2}$ = 360 nm, RSD_2 = 6.6%, $L_{av,3}$ = 570 nm, RSD_3 = 15%. As a result of decoration, the length of both the shortest particles ($L_{av,1}$) and the TMV monomers ($L_{av,2}$) increased marginally. The average length of the longest particles ($L_{av,3}$) apparently decreased, which may correspond to the detachment of some multimeric particles from the surface. As can be seen from the histogram presented in Fig. 2B', the height of the decorated particles follows a single and narrow (RSD = 5.5%) distribution centered on an average height value H_{av} = 42 nm. The H, L correlation plot presented in Fig. 2C' shows that the height and length of decorated particles are not significantly correlated (r = 0.097). Taken together, these results evidence that *decoration of the particles by the integrated system was successful and independent of their actual length*.

We then addressed the question of the homogeneity of the antibody coating along the TMV particles, by acquiring high resolution, i.e. zoomed-in topography images of individual decorated TMVs. The resulting images, and corresponding cross-sections, such as the one presented in Fig. 1B(ii), evidenced the absence of defects in the IgG coating, at least at the scale of a few tens of nanometers.

3.3. Single particle scale Mt/AFM-SECM imaging of the catalytic activity of TMV_{Cys} decorated with the Fc-PEG/PQQ-GDH system

SiO_2 surfaces bearing random arrays of TMV_{Cys} particles decorated with the Fc-PEG/PQQ-GDH system were imaged in Tris-HCl buffer pH 7.5 by tapping mode Mt/AFM-SECM, in the presence of 10 mM glucose. A home-prepared soft AFM-SECM probe was biased at a potential of + 0.3 V/SCE (i.e. ~0.15 V anodic vs. the standard potential of the Fc heads), acoustically oscillated at ~10 nm amplitude, and raster scanned along the surface. The surface topography and tip current were recorded simultaneously and plotted as associated images, as exemplified in Fig. 3 and Fig. S2.

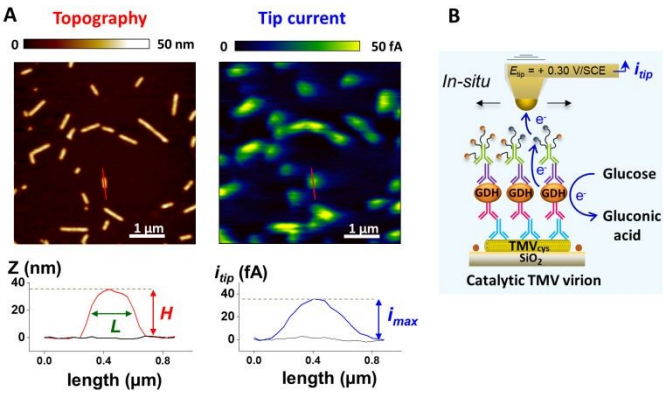

Fig. 3. Mt/AFM-SECM imaging of TMV_{Cys} particles decorated with the Fc-PEG/PQQ-GDH integrated system. **(A)** Simultaneously acquired topography and tip current images. Profiles taken along an isolated individual virion are shown. Imaging buffer: Tris-HCl pH 7.5 containing 10 mM glucose. Tip potential E_{tip} = + 0.3 V/SCE. **(B)** Schematic representation of the electrocatalytic processes triggered by the tip when in contact with a decorated virion particle. Data acquired using soft AFM-SECM tips.

Several individual decorated TMV_{Cys} particles can be identified clearly in the topography image. Of importance, every single one can be associated with a well-defined spot appearing in the current image. Besides, no such current spots were visible if glucose was absent from the imaging buffer (see Fig. S3), or if the enzyme, or the IgG-PEG-Fc, were omitted from the immunoconstruct. The current spots can therefore be assigned to the tip-triggered electrocatalytic activity of the integrated system borne by each TMV particle, as represented schematically in Fig. 3B. The anodically biased tip locally oxidizes the Fc heads into Fc^+, which act as efficient enzymatic cosubstrates for glucose-reduced PQQ-GDH enzyme molecules.[55]

Most interestingly, the broad length distribution of TMV_{Cys}, from incomplete to monomeric and multimeric particles, gave us the unique opportunity of studying the relation between the particles' lengths and their catalytic activities. We therefore analyzed several Mt/AFM-SECM images, measuring the length and height of 122 individual particles, together with the maximum intensity of their associated current spot, i_{max}. These measurements were made from cross-sections of the topographic and current images taken along the contour length of the particles, as defined from the topography images (Fig. 3A). We were then able to construct length, height and current histograms for the decorated TMV, as shown in Fig. 4A, Fig. 4B and Fig. 4C, respectively.

The three populations of TMV_{Cys} can be identified from the length histogram and are characterized by the following parameters: $L_{av,1}$ = 220 nm, RSD_1 = 17%, $L_{av,2}$ = 400 nm, RSD_2 = 11%, $L_{av,3}$ = 695 nm, RSD_3 = 4%. These later values are essentially the same as those measured in the AFM-only experiments for decorated TMV and reported above. Only the distribution of the longer, multimeric, particles differs significantly from the results reported in Fig. 2A'. Their average length increased, most likely due to some loss of shorter head-to-tail aggregates.

Importantly, a unimodal height distribution is obtained (Fig. 4B), yielding an average height for the decorated particles of 42 nm, and a relative standard dispersion of 8%. This average height value is identical to the one obtained in AFM-only experiments, and typical of decorated TMV particles, while the height distribution is narrower for Mt/AFM-SECM than for AFM measurements.

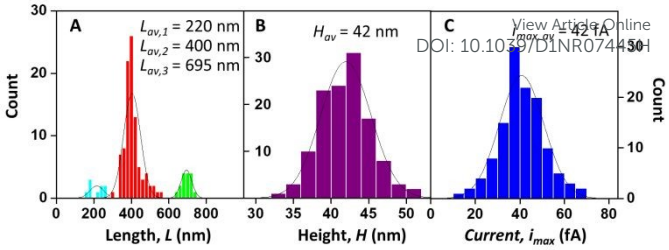

Fig. 4. Statistical distribution of the geometric and catalytic properties of Fc-PEG/PQQ-GDH decorated TMV-scaffolds as reflected by histograms of their: **(A)** length, *L*; **(B)** height, *H*; and **(C)** catalytic tip current intensity, i_{max}. Imaging buffer Tris-HCl pH 7.5 containing 10 mM glucose. E_{tip} = + 0.3 V/SCE. Data acquired for 122 individual particles.

The major interest of the Mt/AFM-SECM experiments was to measure tip current simultaneously with topography data, which rendered uniquely possible to build the catalytic tip current histogram presented in Fig. 4C. A unimodal tip current distribution was obtained. It is characterized by an average catalytic tip current of 42 fA and a relative standard deviation of 25%. This deviation is broader than what can be justified by the experimental errors on our current measurements, which we estimated to be in the order of ± 5 fA and would result here in a RSD of ~12%. Hence, the measured dispersion of catalytic tip current largely translates the actual distribution of the catalytic properties of the particles within their global population, a fundamental property uniquely measurable thanks to the single particle resolution of AFM-SECM.

Moreover, as the Mt/AFM-SECM enables all three *L*, *H* and i_{max} values to be measured for *every single* decorated TMV_{Cys} particle interrogated, one can search for possible correlations between these parameters, simply by plotting one parameter as a function of another, as shown in Fig. 5.

In Fig. 5A, the height of each of the 122 particles sampled is plotted as a function of their respective length. The broad scattering of the data and a low value of the Pearson's coefficient of 0.21 point to a negligible correlation between the particle height and length.

Fig. 5B shows that the catalytic tip current is totally uncorrelated with the particle height. At the opposite, a clearly positive global correlation between the catalytic tip current and particle length is observed, as obvious from Fig. 5C. The strength of this correlation is quantified by a value of r = 0.63, while its statistical significance is ascertained by a statistical p value of p

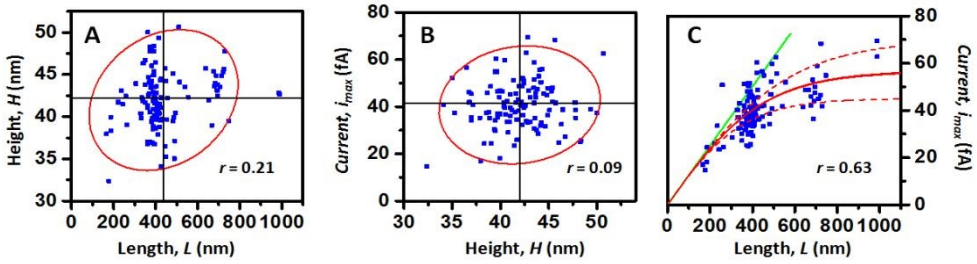

Fig. 5. Cross-correlation plots of the geometric and catalytic parameters of Fc-PEG/PQQ-GDH-decorated *TMV*-scaffolds. The length *L*, height, *H*, and catalytic tip current i_{max} parameters, measured for each of the 122 particles interrogated, are plotted two by two as a function of each other: **(A)** shows the dependence of *H* on *L*, **(B)** and **(C)** show the dependence of i_{max} on *H* and *L*, respectively. 95% confidence ellipses are shown in (A) and (B). *r* is Pearson's correlation coefficient of the data. The green line in (C) is a linear fit of the data in the L < 400 nm region yielding $\gamma_0 k$ = 10^{-21} mol nm^{-1} s^{-1}. The red curves in (C) are calculated using eqn (1) with k/D_e as the sole adjustable parameter. The solid curve is the best fit curve, yielding k/D_e = 10^9 cm^{-2}. Upper and lower dashed curves are calculated with forced values of k/D_e = 0.7 10^9 cm^{-2} and 1.8 10^9 cm^{-2}, respectively. Imaging buffer Tris-HCl pH 7.5 containing 10 mM glucose. E_{tip} = + 0.3 V/SCE.

$< 10^{-5}$, which is much lower than the conventional significance threshold of $p < 0.05$. Yet, more careful examination of the data presented in Fig. 5C actually reveals two *L* regions where the i_{max} vs. *L* correlation visibly differs: in the $L \leq 400$ nm region, encompassing the apparent length of the monomeric TMV particles and shorter, i_{max} and *L* are very strongly correlated linearly (green line in Fig. 5C), with $r = 0.98$. At the opposite, in the $L > 400$ nm region, correlation becomes much weaker, to the point where i_{max} becomes seemingly *L*-independent.

As a control we made sure that the catalytic tip current of the particles did neither depend on their orientation versus the scan direction (Fig. S4), nor was a function of the image scan rate (provided it was kept at, or below 0.3 line/s). These results confirm that the particle length dependence of the tip current we revealed here is not due to a scanning artifact, but rather is a consistent phenomenon, which can be rationalized as follows.

3.4. Understanding the particle-length dependence of the catalytic activity of viral particles: 1D electron hopping coupled to enzymatic reaction.

The above tip current vs. particle length behavior can be fully explained by considering the occurrence of lateral propagation of the Fc^+ heads along the viral particles, driven by electron exchange between neighboring Fc / Fc^+ heads and coupled to the enzymatic reaction, as depicted in Fig. 6: Fc^+ heads are generated at the location where the tip actually "contacts" the particle and swinging motion of the Fc-PEG chains then favors the encounter and electron transfer between Fc^+ and Fc heads. As a result, Fc^+ species formally propagate away from the tip until they are ultimately consumed by the enzymatic reaction. Such kind of hopping-based electron transport mechanism is commonly observed in redox polymers,[73] and typically described as a diffusional process; [74] its coupling to enzymatic reactions is also very well documented.[75] In particular, PEG-borne Fc heads have shown to be capable of shuttling electrons over several hundreds of nanometer across bio-assemblies,[72,76] via a combination of physical elastic motion of the chain and electron hopping between the redox heads.

As detailed in our previous paper,[55] for elongated particles decorated with the Fc-PEG/PQQ-GDH system, coupling between electron diffusion and enzymatic reaction can be described by a simple 1D diffusion/reaction model. Such a model assumes that the decorated viral particles display homogeneous electron transport and enzymatic properties. This assumption is justified here by the homogeneity of the antibody coverage of the TMV_{Cys} scaffold evidenced by the zoomed-in AFM image displayed in Fig. 1B(ii).

The 1D formulation of the problem allows deriving the following analytical expression for the maximum tip current, i_{max}, measured at the center of a particle of length *L*:[55]

$$i_{max} = i^* tanh\left(0.5\, L\sqrt{k/D_e}\right) \quad (1)$$

With $i^* = 2F\gamma_0\sqrt{kD_e}$, where *k* is a pseudo first order constant describing globally the enzyme kinetics, D_e is an effective electron diffusion coefficient and γ_0 the linear concentration of Fc heads along the virus (e.g. in number of Fc heads per nm).

Eqn (1) fully captures the particle length dependence of the catalytic current.

Depending on the respective rates of the enzymatic reaction, *k*, and of electron diffusion along the virus full length, D_e/L^2, two limiting case situations can be identified.

- If electron propagation along the particles is fast with respect to enzymatic catalysis, i.e. $L\sqrt{k/D_e} \ll 1$, eqn (1) simplifies to: $i_{max} = F\gamma_0 kL$ (2)

In this case, the Fc^+ species rapidly propagates from the tip along the virion and reaches all enzyme molecules present on the particle. The catalytic tip current is then solely set by the kinetics of the enzymatic reaction. For any given *k* and D_e values, this situation is expected to be met for sufficiently short virus particles. As seen from eqn (2), a linear i_{max} vs. *L* variation is then expected. This is precisely what is experimentally observed here for $L \leq 400$ nm.

- If, at the opposite, electron propagation along the particles is slow with respect to enzymatic catalysis, i.e. $L\sqrt{k/D_e} \gg 1$, a condition always met for sufficiently long viral particles, Equation 1 reduces to:

$$i_{max} = 2F\gamma_0\sqrt{kD_e} \quad (3)$$

In this case Fc^+ produced at the tip is rapidly consumed by the enzyme molecules located the nearest to it, and does not propagate *all along* the virion. i_{max} consequently becomes length-independent, Equation (3). This is in agreement with the experimental behavior observed for $L \geq 400$ nm.

More quantitatively, by measuring the slope of the linear i_{max} vs. *L* variation observed for $L \leq 400$ nm in Fig. 5C, a value of $(1 \pm 0.2)\ 10^{-21}$ mol nm^{-1} s^{-1} can be obtained for the $\gamma_0 k$ product using Equation 2. It is then possible to fit the i_{max} vs *L* data over the full *L* region explored, using Equation 1 with a single adjustable parameter, the k/D_e ratio. As seen in Fig. 5C (solid red trace), this allows the transition from the linear to the plateau region of the experimental i_{max} vs. *L* variation to be reasonably well reproduced with a best fit value of $k/D_e = (1.2 \pm 0.4)\ 10^9$ cm^{-2} (or equivalently $(1.2 \pm 0.4)\ 10^{-5}$ nm^{-2}). Individual values for *k* and D_e can then be derived from the global parameters k/D_e and $\gamma_0 k$ as detailed below.

The value of γ_0 was determined electrochemically by assaying the amount of Fc heads borne by decorated TMV forming a random array of known virus coverage on a gold surface, as described in ESI (Fig. S5). A typical value of $\gamma_0 = (5 \pm 0.5)$ Fc head per nanometer length of TMV was found. From the $\gamma_0 k$ product, one thus obtains: $k = (120 \pm 40)$ s^{-1}. The

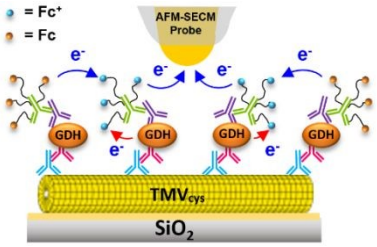

Fig. 6. Schematic representation of the electron hopping process coupled to GDH activity taking place on decorated viral capsids. The AFM-SECM probe (tip) locally oxidizes Fc heads into Fc^+, which exchange electrons with neighboring Fc heads. As a result, Fc^+ formally propagate along the viral particle away from the tip position. Equivalently, electrons are shuttled towards the tip (blue arrows). Competitively to their propagation, Fc^+ heads also serve as enzymatic cofactors for PQQ-GDH (red arrows).

View Article Online
DOI: 10.1039/D1NR07445H

experimental k/D_e value then yields a value of D_e = (1.1 ± 0.4) 10^{-7} cm^2 s^{-1}, which is close to the value of 1.5 10^{-7} cm^2 s^{-1} we determined previously for *fd*-particles decorated with the very same Fc-PEG/PQQ-GDH integrated system.[55] Recalling that the rate of electron transport by combined elastic motion and electron hopping within immuno-assemblies is highly dependent on the spatial organization of the assembly,[72,76] such a result confirms that the Fc-PEG/PQQ-GDH system is structurally identical, irrespective of whether it is scaffolded on *fd* or TMV.

Regarding the value derived here for *k*, one should first emphasize that *k* is a pseudo first order rate constant which does not correspond to any of the individual rate constants involved in the complex reaction scheme describing the PQQ-GDH-catalyzed oxidation of glucose, which we will detail later on. A theoretical expression for *k* is derived in ESI, taking into account the full kinetic mechanism of PQQ-GDH action.

Finally, it is worth pointing out that the seemingly paradoxical *absence* of particle length dependence of the catalytic tip current we previously reported for the *fd*-scaffolded Fc-PEG/PQQ-GDH system[55] is fully coherent with the results we report here for the TMV-scaffolds. Indeed, Fig. 5C reveals that in the 800 nm to 900 nm length range, equivalent to the narrow length distribution of the *fd* bacteriophage particles, i_{max} was experimentally observed to be *L*-independent for the TMV system as well.

At this stage we thus have demonstrated that the catalytic tip current vs. particle length dependence for the TMV-scaffolded Fc-PEG/PQQ-GDH system results from the coupling between electron propagation along the scaffolds with the enzymatic reaction. We showed that this dependence can be quantitatively accounted for by our simple 1D diffusion/reaction model for the whole range of the viral particle length explored. Yet, so far, we considered enzymatic catalysis as being described by a pseudo first order regime. This over-simplification was required to analyze the length dependence of i_{max}, but is of course insufficient when it comes to investigating the kinetic behavior of the virion-supported enzyme. Extracting kinetic information from the tip catalytic current is nevertheless possible, but requires the additional investigations reported below.

3.5. Kinetic characterization of TMV-scaffolded PQQ-GDH. Revealing a scaffold-type effect

The catalytic action of PQQ-GDH involves sequential reactions with the glucose substrate and the Fc cosubstrate.[77,78] To characterize the kinetic behavior of TMV-borne PQQ-GDH, we need to study the dependence of the catalytic tip current on the concentration of the enzyme substrate and/or cosubstrate (glucose and/or Fc^+). But, in order to probe the modulation of i_{max} specifically by the concentration of these species, and not by the particle length, this study has to be carried out within a single TMV-particle population where *L* dispersion is minimal. This condition naturally points to the population of monomeric TMV particles. Choosing this population brings along another benefit: as can be seen in Fig. 5C, the corresponding data points fall into the $L \leq 400$ nm region where the catalytic current is simply proportional to the enzymatic rate, with no interference from the rate of electron propagation. This greatly simplifies extracting kinetic information from the catalytic tip current.

Studying the dependence of the enzymatic activity on Fc^+ concentration can be simply achieved by modulating the tip potential, while recording the activity for individual particles (Fig. S6). The resulting S-shaped kinetic curve (Fig. S8), centered around a potential close to the standard potential of the Fc/Fc+ couple ($E°$ = + 0.15 V/SCE), confirms the role of the Fc-head as the sole redox co-substrate of the enzyme. This curve also contains information regarding enzyme kinetics, but cannot be

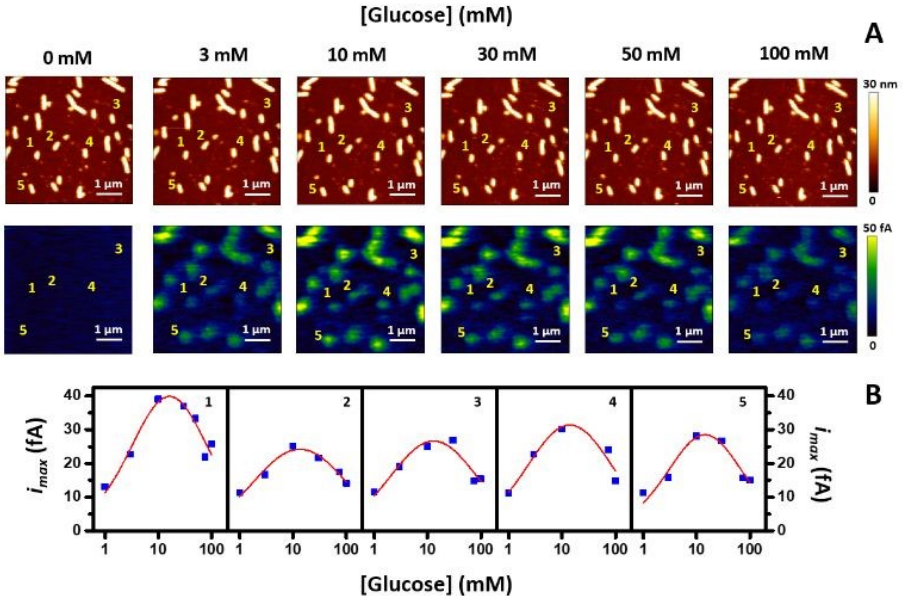

Fig. 7. (A) Mt/AFM-SECM images of individual Fc-PEG/PQQ-GDH-decorated TMV_{Cys} particles recorded at increasing glucose concentrations, as indicated on the top of the images. The very same virions were imaged recursively after incremental injections of glucose. Five particles belonging to the monomeric TMV population were selected and labelled from 1 to 5 as shown. (B) Kinetic plots showing the variation of the catalytic tip current, i_{max}, as a function of glucose concentration for each of the five indexed particles. The red curves are guides to the eyes. The images were acquired in Tris-HCl buffer pH 7.5, using an AFM-SECM soft tip. E_{tip} = + 0.3 V/SCE

analyzed quantitatively without making assumptions about the rate of Fc^+ generation by the tip. We therefore decided to study in detail the dependence of the catalytic current on the glucose concentration.

Mt/AFM-SECM images of an array of decorated TMV_{Cys} were acquired in a Tris-HCl buffer solution into which glucose was progressively added between each scan. The resulting series of topographic and current images is shown in Fig. 7.

The very same decorated TMV particles can be recognized in all of the successively acquired topography images. Five of them, in the monomeric TMV population, were labelled from 1 to 5. Upon glucose injection, current spots appear in the current images at positions corresponding to all virions visible in the topography images. The intensity of the spots is seen to initially increase with glucose concentration, up to a concentration of 10 mM, and to subsequently decrease with further addition of glucose. This trend is visualized better in the plots shown below the images, where the intensity of the catalytic current, i_{max}, recorded for particles 1-5, is plotted as a function of the glucose concentration. A bell-shaped i_{max} vs. glucose variation is observed for all particles. This translates the well-known substrate inhibition of PQQ-GDH. The degree of similarity of the i_{max} vs. glucose variations measured for the 5 particles is hard to assess from the raw data plots presented in Fig. 7. We thus constructed cross-correlation plots shown in Fig. 8, by plotting the values measured for the virions as a function of each other. In spite of some scattering, it is seen that the data tend to align on straight lines passing through the origin. This indicates that the i_{max} vs. glucose variations recorded for the 5 particles are approximately proportional to each other.

At this stage, it is necessary to recall the general expression for the catalytic rate of PQQ-GDH, formally valid for both the non-cooperative and cooperative kinetic modes of this enzyme:[78]

$$v_{ez} \propto {}^{n_E}\Big/\left[\left(1+K_i C_g^0\right)\Big/\left(k_{ox}\,[Fc^+]\right)+\left(1+\frac{K_M}{C_g^0}\right)\Big/k_{cat}\right] \quad (4)$$

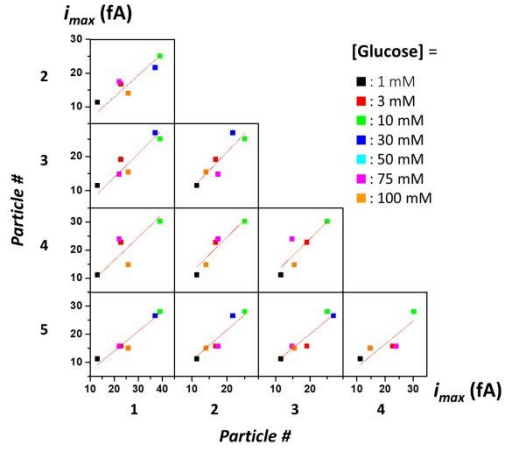

Fig. 8. Cross-correlation plots where the catalytic tip current, i_{max}, of the particles labelled 1-5 in Fig. 7 are plotted as a function of each other, for every glucose concentration value explored. Red traces are least square regression lines passing through the origin.

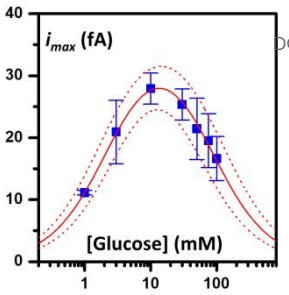

Fig. 9. Kinetic curve characterizing the catalytic activity of the TMV-scaffolded Fc-PEG/PQQ-GDH integrated system: Dependence of i_{max} on the glucose concentration in solution. The curves in red are best fits of eqn (5) to the data, either considering the raw data values (solid line), or the set of boundary values corresponding to ± the error margin (95% confidence interval, dotted lines).

where n_E is the number of PQQ-GDH molecules involved, $[Fc^+]$ the "local" Fc^+ concentration and $C°g$ the bulk glucose concentration. k_{cat} is the catalytic constant of the enzyme, K_M the Michaelis-Menten constant for glucose, k_{ox} the second-order rate constant corresponding to the oxidation of the enzyme by Fc^+, and K_i the equilibrium constant of the enzyme inhibition by glucose.

From Equation 4, it appears that the simple proportionality observed between the catalytic response of different decorated TMV particles exposed to varying concentrations of either glucose, or Fc^+ (see ESI), implies that the PQQ-GDH molecules borne by all virions not only follow the same rate law, but are also characterized by the same rate constant values. It is thus legitimate to average the i_{max} vs. glucose data points recorded for the five particles identified in Fig. 7, in order to obtain the representative kinetic curve presented in Fig. 9**,** which can be analyzed as follows.

Since, for the chosen viral population the catalytic tip current is under the kinetic control of the enzymatic reaction, i_{max} is simply proportional to the enzymatic rate and is therefore given by:

$$i_{max} = {}^{2Fn_E k_{ox}\gamma_0}\Big/\left[\left(1+K_i C_g^0\right)+\frac{k_{ox}\gamma_0}{k_{cat}}\left(1+\frac{K_M}{C_g^0}\right)\right] \quad (5)$$

where n_E is the average number of enzyme molecules on the TMV virions.

Equation 5 could be directly used to fit the kinetic curve presented in Fig. 9, using four adjustable global parameters: n_E $k_{ox}\gamma_0$, $k_{ox}\gamma_0/k_{cat}$, K_i, K_M. Yet, we observed that multiple combinations of these parameters enable to fit the data equally well, preventing the unambiguous determination of their individual values. However, we also observed that, if any value was assigned to the critical parameter $k_{ox}\gamma_0/k_{cat}$ the fitting process led to a unique set of values for the three other parameters, which depended only on the exact value taken for $k_{ox}\gamma_0/k_{cat}$. We thus assigned to $k_{ox}\gamma_0/k_{cat}$"reasonable" test values in the 0.3-0.5 interval, corresponding to the range of values measured for this parameter for the *fd*-scaffolded Fc-PEG/PQQ-GDH system probed at the ensemble or individual particle scale.[51] This led to the very good adjustment of Equation 5 to the data shown in Fig. 9 (solid red trace), and to

View Article Online
DOI: 10.1039/D1NR07445H

the determination of the following range of best fit values: n_E $k_{ox}\gamma_0$= (2.9 ± 1) 10^{-19} mol s^{-1}, K_i = (20 ± 5) M^{-1}, K_M = (9 ± 3) mM.

In order to determine the missing n_E value, we experimentally measured the linear coverage of TMV virions by the PQQ-GDH enzyme, and found a coverage γ_E = 0.1 ± 0.02 PQQ-GDH molecule per nanometer length of virus (see ESI). Hence, the average number of active PQQ-GDH molecules decorating the monomeric TMV particles considered here, which had an experimental average length of 400 nm, can be estimated as: n_E = 400 γ_E = 40 ± 10. This yields $k_{ox}\gamma_0$ = (5 ± 2.5) 10^3 s^{-1}, and, taking an intermediate value of 0.4 for the $k_{ox}\gamma_0/k_{cat}$ parameter we find: k_{cat} = (12.5 ± 6) 10^3 s^{-1}. The kinetic data determined for the TMV-scaffolded integrated system are collected in Table 1 and compared to values previously obtained for the *fd*-scaffolded system. Also reported in Table 1 are the kinetic parameters characterizing the activity of PQQ-GDH in solution in both of its kinetic modes. It can be seen that the k_{cat} and K_M parameters for the TMV-scaffolded system are very comparable to those typical of PQQ-GDH in its *cooperative* kinetic mode in solution, showing that in the integrated system the enzyme spontaneously adopts its fastest mode. This is a beneficial effect of scaffolding which we also observed for the *fd*-confined Fc-PEG/PQQ-GDH system.[51] Indeed, as seen in Table 1, the sets of k_{cat} and K_M values measured for both of the viral scaffolds are very similar to each other. One can thus conclude that this particular catalytic "enhancement" effect of nanoscaffolding is independent of the exact nature of the virion, suggesting that it is simply related to the nanometer–size of the scaffolds. Confinement of the Fc-PEG chains on the nanoscaffold yields an increased local mediator concentration around the enzyme molecules, which results in PQQ-GDH adopting its cooperative kinetic mode, as observed in solution when the cosubstrate concentration is high.[77] Yet, Table 1 also reveals that, surprisingly, the K_i values differ significantly from one viral scaffold to the other: whereas the K_i value found for the *fd*-supported system is close to that reported for PQQ-GDH in solution, the value derived for the TMV-supported system is 4.5 times lower. The actual reasons for the here-observed scaffold-type effect are likely rooted in some differences in the microenvironment of the enzyme borne by either the *fd*- or TMV-particles. In that respect, the effect of local electric charge is worth discussing since this parameter has been shown to modulate the activity of enzymes assembled on charged scaffolds such as DNA,[39,44,50] or even entrapped within hollow viral particles.[23]

In the present case, *fd* and TMV bear differing (negative) electric charges at the working pH: *fd* carries a linear charge of 10 e^-/nm at pH 7.4 (total charge 8800 e^-)[83] whereas the estimated linear charge of TMV is only ~3e^-/nm at most (total nominal charge ~1000e^-).[68,84,85]One also has to take into account the charges carried by the antibodies of the immuno-construct. Considering that: (*i*) at pH 7.5 each antibody carries from 5 to 10 negative charges,[86] (*ii*) there are 4 antibodies per GDH in the construct, (*iii*) the linear coverage of GDH on the virions was in the order of 0.1-0.2 GDH/nm, one calculates an extra linear charge density due to the IgGs of 2-8 e^-/nm. Overall, comparable total charge densities of 12-18 e^-/nm and 5-11 e^-/nm are derived for the fully decorated *fd* and TMV, respectively. It follows that dissimilarity in the electric charge experienced by the enzyme can hardly account for the difference in K_i between the *fd*- and TMV-systems. However, there is more to the microenvironment of scaffolded enzymes than mere electric charge, and non-charge-based molecular interactions between the enzyme *substrate* and the scaffold can also alter the kinetic behavior of scaffolded enzymes.[45,48–50] When such interactions exist, the local substrate concentration is modified and consequently the kinetic constants reflecting the dependence of enzyme activity on the substrate concentration are affected. Differences in binding interactions between the scaffold and glucose could thus *a priori* account for different K_i values between the two viral scaffolds. However, such a substrate binding effect would also be expected to yield differing K_M values, which is not the case. Hence, it is likely that a more complex mechanism underlies the scaffold-type dependent substrate inhibition of PQQ-GDH evidenced here. This result is in line with the many cases of catalytic enhancement reported in the literature, for which no clear mechanism has been identified yet. [45]

3.6. Pushing the limits of electrochemical imaging of enzymatic activity at the nanoscale: two domain-TMV-like particles (DTLPs).

Our Mt/AFM-SECM study of a viral particle-supported enzymatic system provides a unique benchmark to explore the limits of probing enzymatic activity by electrochemical imaging.

Table 1. Set of kinetic constants characterizing the catalytic activity of PQQ-GDH in various configurations, as indicated. The first two columns present single particle Mt/AFM-SECM data for the *TMV- and fd-* scaffolded Fc-PEG/PQQ-GDH systems, respectively. N.A. = non applicable.

Enzymatic constants	TMV-scaffolded system Mt/AFM-SECM (This work)	fd-scaffolded system Mt/AFM-SECM (Ref. [55])	GDH in solution Fc in solution Coop. mode (Ref. [78])	GDH in solution Fc in solution Non-coop. mode
k_{cat} (s^{-1})	12500 ± 6000	10000 ± 4000	6000 ± 1000	1500 ± 300
K_M (mM)	9 ± 3	8 ± 3	4.7 ± 0.3	0.27 ± 0.005
K_i (M^{-1})	20 ± 5	90 ± 35	127 ± 20	52 ± 6
k_{ox} γ_0 (s^{-1})	5000 ± 2500	5000 ± 2000	N.A.	N.A.

To tackle this issue, we turned to a composite viral nanoscaffold: TMV-like particles (TLPs) composed of two sequential longitudinal domains of pre-defined length, displaying distinct epitopes. This domain-TLP (DTLP) scaffold, produced by an original dynamic DNA-controlled *in vitro* assembly technology,[62] is represented schematically in Fig. 10B. It is composed of a main 5'-domain (5' with respect to the RNA template inside) of cysteine-exposing coat proteins (CP_{Cys}, in yellow), ~ 260 nm in nominal length, and of a 40 nm-long 3'-terminal domain of CP_{Cys} covalently functionalized by biotin moieties ($CP_{Cys\text{-}bio}$, in green).

These DTLPs were adsorbed on an aminated SiO_2 surface and immuno-decorated with Fc-PEG/PQQ-GDH as described in Fig. 1, except that the DTLP array was exposed to anti-biotin IgGs instead of anti-TMV CP IgGs. As a result, the antibodies were expected to be selectively immobilized on the short 40 nm biotinylated terminal DTLP domain, as depicted in Fig. 10B. Zoomed-in Mt/AFM-SECM images of the decorated DTLP were then acquired in the presence of 10 mM glucose in the imaging buffer, Fig. 10A and Fig. S10.

In Fig. 10, an individual apparently ~400 nm long DTLP is recognized in the topography image. It displays a distinct high contrast area at only one of its extremities. This feature, never observed for homogeneously functionalized TMV particles, can be better examined in the topography profile taken along the virus axis and reproduced below the images. One can see that it corresponds to an apparently ~100 nm long terminal region of the virion, whose height appears increased by 4 nm with respect to the rest of the capsid.

The simultaneously recorded current image shows a single spot, the position of which coincides with the thickened extremity of the decorated DTLP. Importantly, the tip current is detected only at this extremity of the viral particle and nowhere else along the viral capsid. The corresponding broad and bell-shaped ~10 fA tip current variation is seen best in the superimposed current and topography profiles shown in Fig. 10A. From this, we can conclude that the current is due to the tip triggering and probing the enzymatic activity of PQQ-GDH molecules selectively decorating the short terminal biotinylated DTLP domain. This evidences the successful regio-selective decoration of the DTLP by the integrated system, as depicted in Fig. 10B.

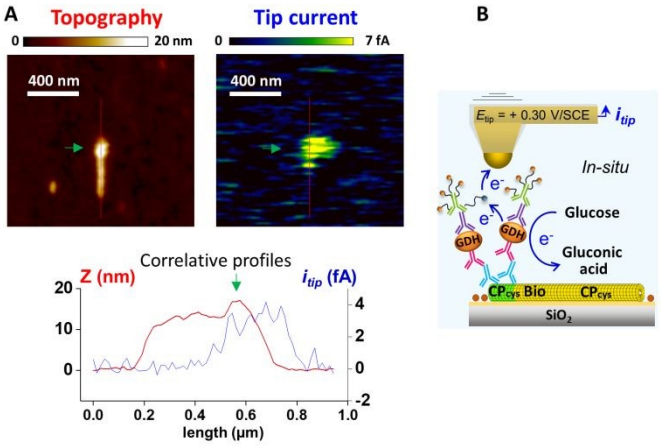

Fig. 10. Mt/AFM-SECM images of an individual $CP_{Cys}/CP_{Cys\text{-}bio}$ DTLP terminally decorated with the Fc-PEG/PQQ-GDH system. **(A)** Topography and tip current images. The green arrow marks the approximate position of the 40 nm long $CP_{Cys\text{-}bio}$ extremity of the viral particle. Topography and current profiles taken along the long axis of the virion as shown, are reproduced below the images. (B) Schematic depiction of the interrogation of the decorated domain by the AFM-SECM tip. Imaging buffer: Tris-HCl pH 7.5 containing 10 mM glucose. E_{tip} = + 0.3 V/SCE.

The fact that in topography, the decorated terminal region appears longer (100 nm) than the biotinylated domain length (40 nm) is likely due to the dimensions of the antibody construct extending each terminus of the biotinylated domain and forming a large hemispherical immunocomplex. The low apparent thickening (by 4 nm) of the decorated terminal DTLP region with respect to the main domain arises from the high flexibility (softness) of this biomolecule complex, which renders it hardly sensed by the tip. As a whole, the particular geometry and flexibility of the complex, together with the delay in the time response of the current measurer, can explain broadening of the current spot, and its slight distortion in the scan direction.

It is most interesting to try to evaluate the number of PQQ-GDH molecules involved in generating such small currents. To this end, one could assume that the number of PQQ-GDH molecules per unit length of the DTLP was 0.1 ± 0.02, as measured above for decorated TMV particles. This would translate into ~5 enzyme molecules decorating the biotinylated domain of the DTLP. This number is probably an underestimation, because the hemispherical geometry of the assembly at the terminal domain likely accommodates more PQQ-GDH molecules than allowed upon "linear" arrangement of antibodies along the TMV capsid. Alternatively, one can also estimate geometrically the number of antibodies that could be accommodated on the biotinylated TMV-based scaffold domain, modeled as a core cylinder of ~9 nm in radius and 40 nm long, and assuming a typical 100 nm^2 footprint for an antibody bound to this scaffold. This simple geometric calculation yields ~20 IgG borne by the 3'-DTLP domain. Hence it seems safe to consider that only a few tens of PQQ-GDH molecules were addressed by the AFM-SECM tip when interrogating the decorated 40 nm segment of the DTLP.

To the best of our knowledge, this sets a new record not only in terms of the smallest number of enzyme molecules functionally probed by an electrochemical microscopy technique, but also for the resolution of the smallest enzymatic domain ever functionally imaged in SECM. Indeed, even though the catalytic activity of inorganic nanoparticles as small as ~10 nm in size has been recently probed by SECM,[87] and related techniques,[88,89] the comparatively slow kinetics of enzymes has so far prevented electrochemical imaging of enzymatic reactions with a resolution better than a few ~100 nm.[59,90] The significantly higher resolution we achieve here with Mt/AFM-SECM comes as a benefit of the mediator-tethered configuration, which prevents diffusional dispersion of the Fc heads, otherwise occurring in classical SECM configurations making use of soluble mediators.[57,91]

DOI: 10.1039/D1NR07445H

4. Conclusions

In this paper, functional nanoscale interrogation of an integrated electro-catalytic system, comprising the PQQ-GDH enzyme and its Fc-PEG redox mediator, co-assembled on a linear TMV-based viral nano-scaffold, was achieved. It revealed a marked length dependence of the tip-triggered catalytic activity of the decorated rod-shaped particles. This finding was explained by the occurrence of electron propagation along the viral backbone, due to electron exchange between neighboring Fc heads, coupled to enzymatic catalysis. The limiting kinetic regimes corresponding to control of the current by the enzymatic reaction either alone, or in conjunction with the electron transport process, could be experimentally observed. A simple 1D diffusion/reaction model described the length dependence of the particles' catalytic response quantitatively, and allowed the kinetic parameters of the virus-supported PQQ-GDH enzyme to be determined. The analysis evidenced two distinct kinetic effects of scaffolding : non-virus-type-dependent enhancement of catalysis due to the enzyme adopting its fastest cooperative kinetic mode, and virus-type-dependent modulation of substrate inhibition.

Important progresses were also made in terms of resolving enzymatic activity at the nanoscale by electrochemical microscopy. *Quantitative* interrogation of decorated TMV particles as short as ~200 nm long was evidenced. Furthermore, detection of the enzymatic activity of PQQ-GDH decorating an only 40 nm long viral domain was possible. The activity of not more than a few tens (or less) enzyme molecules decorating such a nano-domain was probed. This represents the highest spatial resolution ever achieved for the functional interrogation of enzyme molecules by electrochemical microscopy.

Conflicts of interest

There are no conflicts to declare.

Acknowledgements

Dr. Nicolas Mano is thanked for providing the pgp492 plasmid used to produce PQQ-GDH. We thank Drs. Benoit Limoges, François Mavré and Mathieu Branca for the generous gift of a PQQ sample, Rebecca Hummel, Conny Kocher and Laura Herlein for technical support, Annika Allinger and Marvin Müller for plant cultivation, and Claudia Koch, Katharina Hipp and Holger Jeske for scientific support, advice and inspiring discussions.

Notes and references

1 R. D. Milton, T. Wang, K. L. Knoche and S. D. Minteer, *Langmuir*, 2016, **32**, 2291–2301.

2 A. De Poulpiquet, A. Ciaccafava and E. Lojou, *Electrochim. Acta*, 2014, **126**, 104–114.

3 H. Chen, O. Simoska, K. Lim, M. Grattieri, M. Yuan, F. Dong, Y. S. Lee, K. Beaver, S. Weliwatte, E. M. Gaffney and S. D. Minteer, *Chem. Rev.*, 2020, **120**, 12903–12993.

4 S. Ding, A. A. Cargill, I. L. Medintz and J. C. Claussen, *Curr. Opin. Biotechnol.*, 2015, **34**, 242–250.

5 J. N. Vranish, M. G. Ancona, S. A. Walper and I. L. Medintz, *Langmuir*, 2018, **34**, 2901–2925.

6 Y. R. Yang, Y. Liu and H. Yan, *Bioconjug. Chem.*, 2015, **26**, 1381–1395.

7 Y. Hu and C. M. Niemeyer, *Adv. Mater.*, 2019, **31**, 1806294.

8 P. W. K. Rothemund, *Nature*, 2006, **440**, 297–302.

9 D. Cardinale, N. Carette and T. Michon, *Trends Biotechnol.*, 2012, **30**, 369-376.

10 W. F. Rurup, M. S. T. Koay and J. J. L. M. Cornelissen, in *Enzyme Nanocarriers*, eds. D. Cardinale and T. Michon, Pan Stanford Publishing, New York, NY, 2016, pp. 105–122.

11 A. Chatterji, W. Ochoa, L. Shamieh, S. P. Salakian, S. M. Wong, G. Clinton, P. Ghosh, T. Lin and J. E. Johnson, *Bioconjug. Chem.*, 2004, **15**, 807–813.

12 N. Carette, H. Engelkamp, E. Akpa, S. J. Pierre, N. R. Cameron, P. C. M. Christianen, J. C. Maan, J. C. Thies, R. Weberskirch, A. E. Rowan, R. J. M. Nolte, T. Michon and J. C. M. Van Hest, *Nat. Nanotechnol.*, 2007, **2**, 226–229.

13 A. A. A. Aljabali, J. E. Barclay, N. F. Steinmetz, G. P. Lomonossoff and D. J. Evans, *Nanoscale*, 2012, **4**, 5640–5645.

14 J. Pille, D. Cardinale, N. Carette, C. Di Primo, J. Besong-Ndika, J. Walter, H. Lecoq, M. B. van Eldijk, F. C. M. Smits, S. Schoffelen, J. C. M. van Hest, K. Makinen, T. Michon, K. Mäkinen and T. Michon, *Biomacromolecules*, 2013, **14**, 4351–4359.

15 S. Cuenca, C. Mansilla, M. Aguado, C. Yuste-Calvo, F. Sánchez, J. M. Sánchez-Montero and F. Ponz, *Front. Plant Sci.*, 2016, **7**, 464.

16 M. Bäcker, C. Koch, S. Eiben, F. Geiger, F. Eber, H. Gliemann, A. Poghossian, C. Wege, M. J. Schöning and 716–722. Bäcker, M.; Koch, C.; Eiben, S.; Geiger, F.; Eber, F.; Gliemann, H.; Poghossian, A.; Wege, C.; Schöning, M. J. Tobacco Mosaic Virus as Enzyme Nanocarrier for Electrochemical Biosensors. Sensors Actuators, B Chem. 2017, 238, *Sensors Actuators, B Chem.*, 2017, **238**, 716–722.

17 C. Koch, A. Poghossian, M. J. Schöning and C. Wege, *Nanotheranostics*, 2018, **2**, 184–196.

18 A. Poghossian, M. Jablonski, C. Koch, T. S. Bronder, D. Rolka, C. Wege and M. J. Schöning, *Biosens. Bioelectron.*, , DOI:10.1016/j.bios.2018.03.036.

19 J. Röder, R. Fischer and U. Commandeur, *Small*, 2017, **13**, 1702151.

20 J. Schuphan and U. Commandeur, *Front. Plant Sci.*, 2021, **12**, 1481.

21 M. Comellas-Aragonès, H. Engelkamp, V. I. Claessen, N. A. J. M. Sommerdijk, A. E. Rowan, P. C. M. Christianen, J. C. Maan, B. J. M. Verduin, J. J. L. M. Cornelissen and R. J. M. Nolte, *Nat. Nanotechnol.*, 2007, **2**, 635–639.

22 J. D. Fiedler, S. D. Brown, J. L. Lau and M. G. Finn, *Angew. Chem. Int. Ed. Engl.*, 2010, **49**, 9648–9651.

23 J. E. Glasgow, M. A. Asensio, C. M. Jakobson, M. B. Francis and D. Tullman-Ercek, *ACS Synth. Biol.*, 2015, **4**, 1011–1019.

24 L. Schoonen, R. J. M. Nolte and J. C. M. van Hest, *Nanoscale*, 2016, **8**, 14467–14472.
25 P. C. Jordan, D. P. Patterson, K. N. Saboda, E. J. Edwards, H. M. Miettinen, G. Basu, M. C. Thielges and T. Douglas, *Nat Chem*, 2016, **8**, 179–185.
26 P. Gama, R. D. Cadena-Nava, K. Juarez-Moreno, J. Pérez-Robles and R. Vazquez-Duhalt, *ChemMedChem*, 2021, **16**, 1438–1445.
27 A. Rajendran, E. Nakata, S. Nakano and T. Morii, *ChemBioChem*, 2017, **18**, 696–716.
28 M. Vázquez-González, C. Wang and I. Willner, *Nat. Catal.*, 2020, **3**, 256–273.
29 D. P. Patterson, B. Schwarz, R. S. Waters, T. Gedeon and T. Douglas, *ACS Chem. Biol.*, 2014, **9**, 359–365.
30 C. Koch, K. Wabbel, F. J. Eber, P. Krolla-Sidenstein, C. Azucena, H. Gliemann, S. Eiben, F. Geiger and C. Wege, *Front. Plant Sci.*, 2015, **6**, 1137.
31 J. Besong-Ndika, M. Wahlsten, D. Cardinale, J. Pille, J. Walter, T. Michon and K. Mäkinen, *Front. Plant Sci.*, 2016, **7**, 89.
32 M. Brasch, R. M. Putri, M. V. De Ruiter, D. Luque, M. S. T. Koay, J. R. Caston and J. J. L. M. Cornelissen, *J. Am. Chem. Soc.*, 2017, **139**, 1512–1519.
33 J. L. Liu, D. Zabetakis, J. C. Breger, G. P. Anderson and E. R. Goldman, *Front. Bioeng. Biotechnol.*, 2020, **8**, 571.
34 Y. Wang, M. Uchida, H. K. Waghwani and T. Douglas, *ACS Synth. Biol.*, 2020, **9**, 3298–3310.
35 Q. Wei, S. He, J. Qu and J. Xia, *Bioconjug. Chem.*, 2020, **31**, 2413–2420.
36 J. L. Lin, L. Palomec and I. Wheeldon, *ACS Catal.*, 2014, **4**, 505–511.
37 J. M. Sperl and V. Sieber, *ACS Catal.*, 2018, **8**, 2385–2396.
38 E. T. Hwang and S. Lee, *ACS Catal.*, 2019, **9**, 4402–4425.
39 G. A. Ellis, W. P. Klein, G. Lasarte-Aragonés, M. Thakur, S. A. Walper and I. L. Medintz, *ACS Catal.*, 2019, **9**, 10812–10869.
40 I. Wheeldon, S. D. Minteer, S. Banta, S. C. Barton, P. Atanassov and M. Sigman, *Nat. Chem.*, 2016, **8**, 299–309.
41 J. Fu, M. Liu, Y. Liu, N. W. Woodbury and H. Yan, *J Am Chem Soc*, 2012, **134**, 5516–5519.
42 W. P. Klein, R. P. Thomsen, K. B. Turner, S. A. Walper, J. Vranish, J. Kjems, M. G. Ancona and I. L. Medintz, *ACS Nano*, 2019, **13**, 13677–13689.
43 Z. Zhao, J. Fu, S. Dhakal, A. Johnson-Buck, M. Liu, T. Zhang, N. W. Woodbury, Y. Liu, N. G. Walter and H. Yan, *Nat. Commun.*, 2016, **7**, 10619.
44 Y. Zhang, S. Tsitkov and H. Hess, *Nat. Commun.*, 2016, **7**, 13982.
45 L. Lancaster, W. Abdallah, S. Banta and I. Wheeldon, *Chem. Soc. Rev.*, 2018, **47**, 5177–5186.
46 Y. Zhang, Q. Wang and H. Hess, *ACS Catal.*, 2017, **7**, 2047–2051.
47 S. J. Maassen, P. van der Schoot and J. J. L. M. Cornelissen, *Small*, 2018, **14**, 1802081.
48 J. L. Lin and I. Wheeldon, *ACS Catal.*, 2013, **3**, 560–564.
49 Y. Gao, C. C. Roberts, J. Zhu, J.-L. Lin, C. A. Chang and I. Wheeldon, *ACS Catal.*, 2015, **5**, 2149–2153.
50 Y. Gao, C. C. Roberts, A. Toop, C. A. Chang and I. Wheeldon, *ChemBioChem*, 2016, **17**, 1430–1436.
51 K. Torbensen, A. N. Patel, A. Anne, A. Chovin, C. Demaille, L. Bataille, T. Michon and E. Grelet, *ACS Catal.*, 2019, **9**, 5783–5796.
52 J. V. Macpherson and P. R. Unwin, *Anal. Chem.*, 2000, **72**, 276–285.
53 A. Eifert and C. Kranz, *Anal. Chem.*, 2014, **86**, 5190–5200.
54 A. Anne, A. Chovin, C. Demaille and M. Lafouresse, *Anal. Chem.*, 2011, **83**, 7924–7932.
55 T. O. Paiva, K. Torbensen, A. N. Patel, A. Anne, A. Chovin, C. Demaille, L. Bataille and T. Michon, *ACS Catal.*, 2020, **10**, 7843–7856.
56 C. Koch, F. J. Eber, C. Azucena, A. Förste, S. Walheim, T. Schimmel, C. Wege, A. M. Bittner, H. Jeske, H. Gliemann, S. Eiben, F. C. Geiger and C. Wege, *Beilstein J. Nanotechnol.*, 2016, **7**, 613–629.
57 D. T. Pierce, P. R. Unwin and A. J. Bard, *Anal. Chem.*, 1992, **64**, 1795–1804.
58 C. Kranz, G. Wittstock, H. Wohlschläger and W. Schuhmann, *Electrochim. Acta*, 1997, **42**, 3105–3111.
59 A. Kueng, C. Kranz, A. Lugstein, E. Bertagnolli and B. Mizaikoff, *Angew. Chemie - Int. Ed.*, 2003, **42**, 3238–3240.
60 B. R. Horrocks and G. Wittstock, in *Scanning Electrochemical Microscopy Second Edition*, eds. A. J. Bard and M. V. Mirkin, CRC Press, Boca Raton, Second Edi., 2012, pp. 317–378.
61 F. C. Geiger, F. J. Eber, S. Eiben, A. Mueller, H. Jeske, J. P. Spatz and C. Wege, *Nanoscale*, 2013, **5**, 3808–16.
62 A. Schneider, F. J. Eber, N. L. Wenz, K. Altintoprak, H. Jeske, S. Eiben and C. Wege, *Nanoscale*, 2016, **8**, 19853–19866.
63 L. Nault, C. Taofifenua, A. Anne, A. Chovin, C. Demaille, J. Besong-Ndika, D. Cardinale, N. Carette, T. Michon and J. Walter, *ACS Nano*, 2015, **9**, 4911–4924.
64 J. Abbou, C. Demaille, M. Druet and J. Moiroux, *Anal. Chem.*, 2002, **74**, 6355–6363.
65 I. Horcas, R. Fernández, J. M. Gómez-Rodríguez, J. Colchero, J. Gómez-Herrero and A. M. Baro, *Rev. Sci. Instrum.*, 2007, **78**, 013705.
66 C. Wege and C. Koch, *Wiley Interdiscip. Rev. Nanomedicine Nanobiotechnology*, , DOI:10.1002/wnan.1591.
67 P. J. G. Butler, *Philos. Trans. R. Soc. London. Ser. B Biol. Sci.*, 1999, **354**, 537–550.
68 J. M. Alonso, M. L. Górzny and A. M. Bittner, *Trends Biotechnol.*, 2013, 31, 530–538.
69 Z. Wu, A. Mueller, S. Degenhard, S. E. Ruff, F. Geiger, A. M. Bittner, C. Wege and C. E. Krill, *ACS Nano*, 2010, **4**, 4531–4538.
70 Y. L. Jeyachandran, E. Mielczarski, B. Rai and J. A. Mielczarski, *Langmuir*, 2009, **25**, 11614–11620.
71 M. Knez, M. P. Sumser, A. M. Bittner, C. Wege, H. Jeske, D. M. P. Hoffmann, K. Kuhnke and K. Kern, *Langmuir*, 2004, **20**, 441–447.
72 A. Anne, C. Demaille and J. Moiroux, *J. Am. Chem. Soc.*, 1999, **121**, 10379–10388.
73 A. Ruff, *Curr. Opin. Electrochem.*, 2017, **5**, 66–73.
74 D. N. Blauch and J. M. Savéant, *J. Am. Chem. Soc.*, 1992,

View Article Online
DOI: 10.1039/D1NR07445H

114, 3323–3332.
75 A. Heller, *Acc. Chem. Res.*, 1990, **23**, 128–134.
76 A. Anne, C. Demaille and J. Moiroux, *J. Am. Chem. Soc.*, 2001, **123**, 4817–4825.
77 F. Durand, B. B. Limoges, N. Mano, F. Mavré, R. Miranda-Castro, J. M. Savéant, F. Mavré, R. Miranda-Castro and J.-M. Savéant, *J. Am. Chem. Soc.*, 2011, **133**, 12801–12809.
78 L. Zhang, R. Miranda-Castro, C. Stines-Chaumeil, N. Mano, G. Xu, F. Mavré and B. Limoges, *Anal. Chem.*, 2014, **86**, 2257–2267.
79 Y. Zhang, J. Ge and Z. Liu, *ACS Catal.*, 2015, **5**, 4503–4513.
80 P. A. Dickensheets, L. F. Chen and G. T. Tsao, *Biotechnol. Bioeng.*, 1977, **19**, 365–375.
81 D. A. Cowan, R. M. Daniel and H. W. Morgan, *Int. J. Biochem.*, 1987, **19**, 483–486.
82 I. Chiyanzu, D. A. Cowan and S. G. Burton, *J. Mol. Catal. B Enzym.*, 2010, **63**, 109–115.
83 K. Zimmermann, H. Hagedorn, C. C. Heuck, M. Hinrichsen and H. Ludwig, *J. Biol. Chem.*, 1986, **261**, 1653–1655.
84 E. E. Maier, R. Krause, M. Deggelmann, M. Hagenbuechle, R. Weber and S. Fraden, *Macromolecules*, 1992, **25**, 1125–1133.
85 G. A. Bach, A. D. Hollingsworth and D. L. Koch, *J. Colloid Interface Sci.*, 2002, **251**, 208–213.
86 D. Yang, R. Kroe-Barrett, S. Singh and T. Laue, *Antibodies (Basel, Switzerland)*, 2019, **8**, 24.
87 M. V. Mirkin, T. Sun, Y. Yu and M. Zhou, *Acc. Chem. Res.*, 2016, **49**, 2328–2335.
88 C. L. Bentley, M. Kang and P. R. Unwin, *J. Am. Chem. Soc.*, 2017, **139**, 16813–16821.
89 C. L. Bentley, J. Edmondson, G. N. Meloni, D. Perry, V. Shkirskiy and P. R. Unwin, *Anal. Chem.*, 2019, **91**, 84–108.
90 Y. Takahashi, A. I. Shevchuk, P. Novak, B. Babakinejad, J. Macpherson, P. R. Unwin, H. Shiku, J. Gorelik, D. Klenerman, Y. E. Korchev and T. Matsue, *Proc. Natl. Acad. Sci. U. S. A.*, 2012, **109**, 11540–11545.
91 A. Anne, C. Demaille and C. Goyer, *ACS Nano*, 2009, **3**, 819–827.

View Article Online
DOI: 10.1039/D1NR07445H

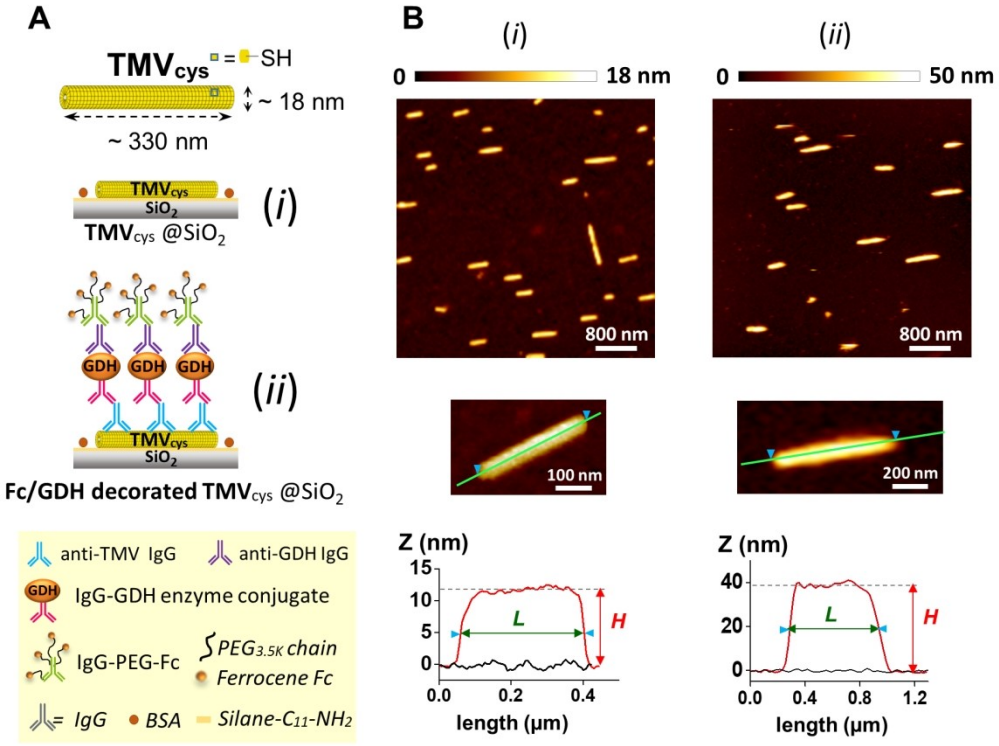

Figure 1

154x115mm (300 x 300 DPI)

View Article Online
DOI: 10.1039/D1NR07445H

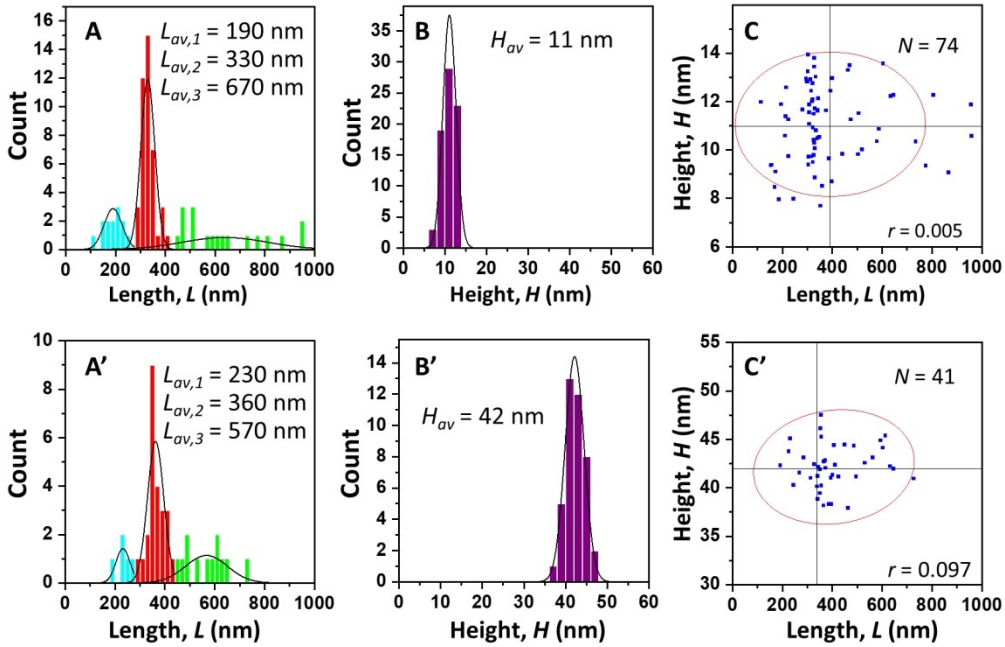

150x100mm (300 x 300 DPI)

View Article Online
DOI: 10.1039/D1NR07445H

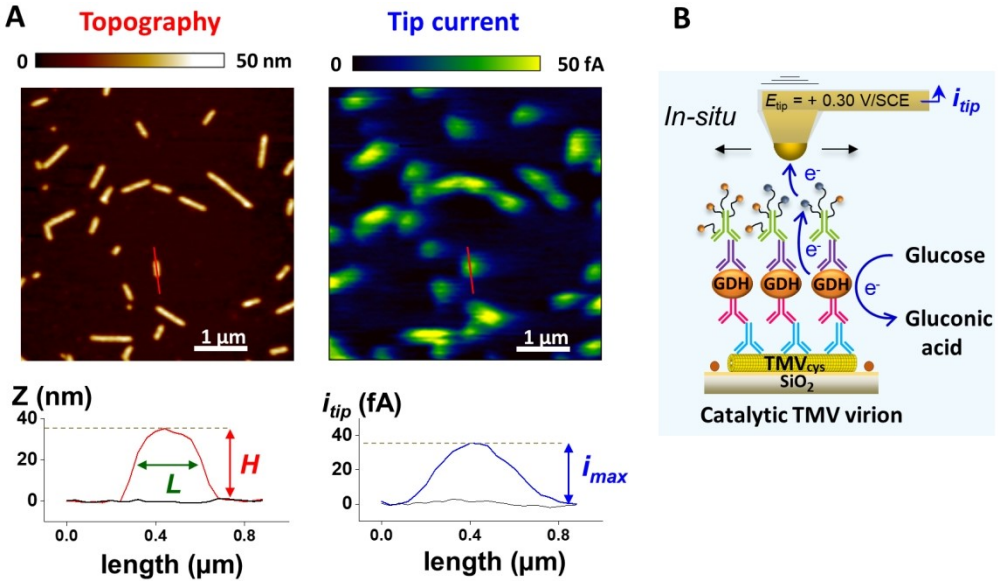

146x84mm (300 x 300 DPI)

View Article Online
DOI: 10.1039/D1NR07445H

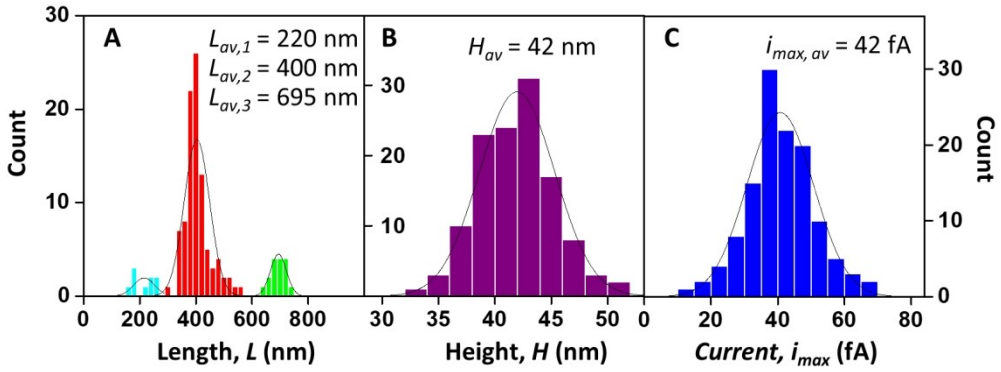

144x53mm (300 x 300 DPI)

View Article Online
DOI: 10.1039/D1NR07445H

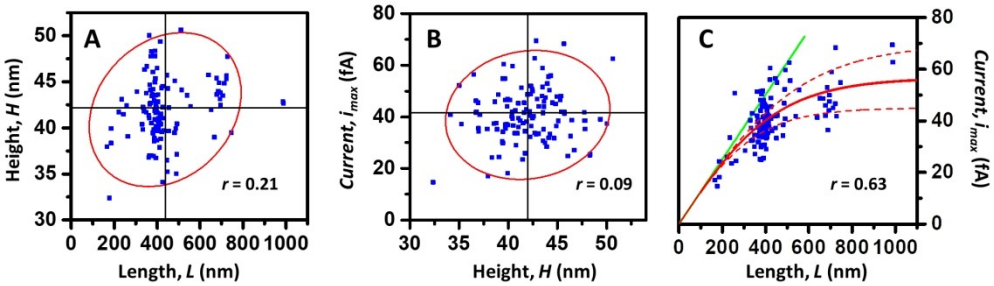

172x48mm (300 x 300 DPI)

View Article Online
DOI: 10.1039/D1NR07445H

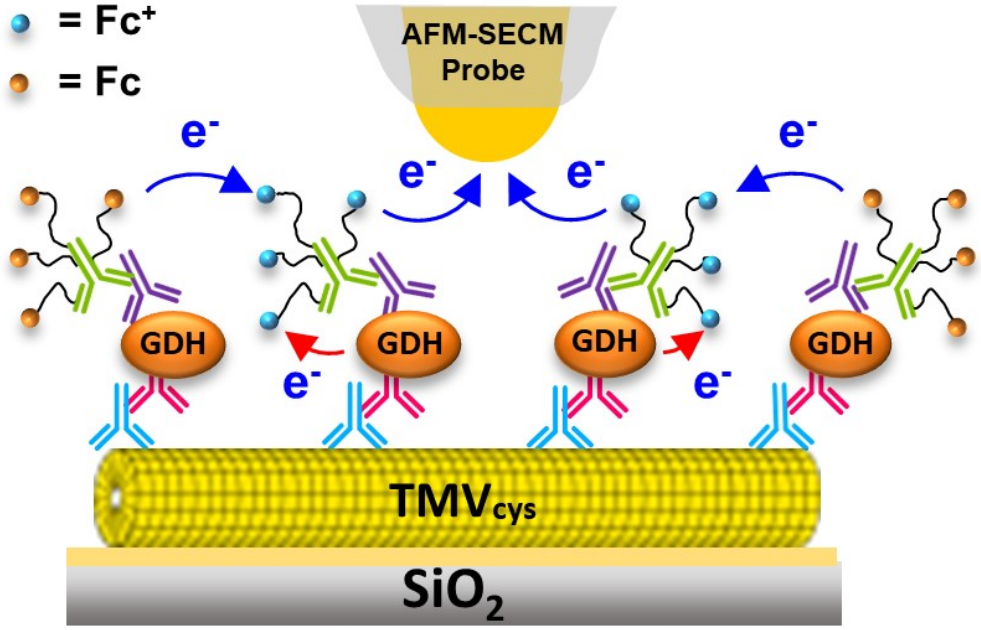

68x44mm (300 x 300 DPI)

View Article Online
DOI: 10.1039/D1NR07445H

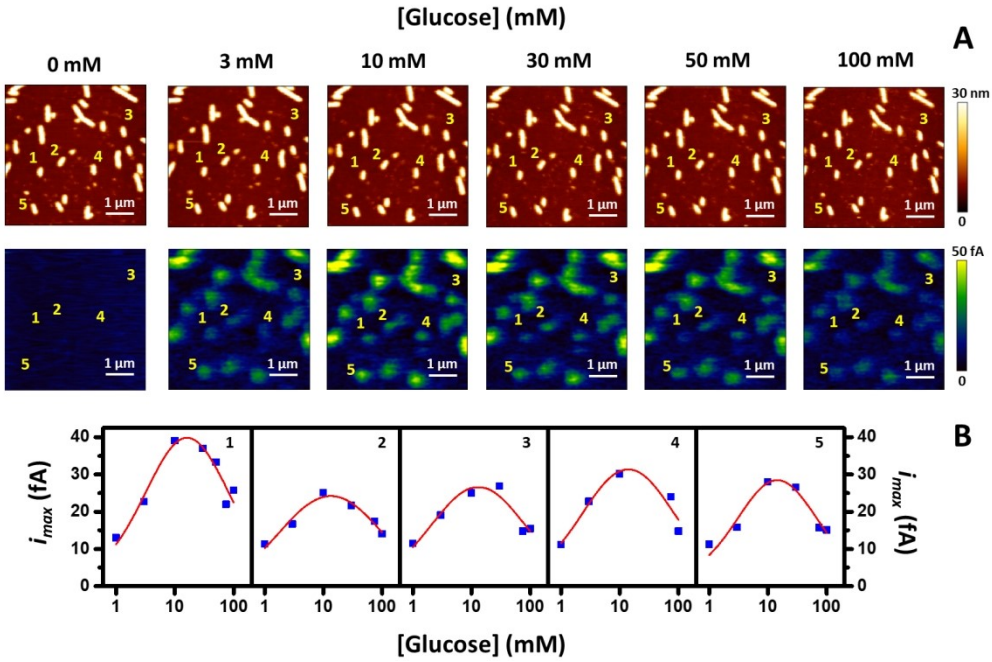

141x93mm (300 x 300 DPI)

View Article Online
DOI: 10.1039/D1NR07445H

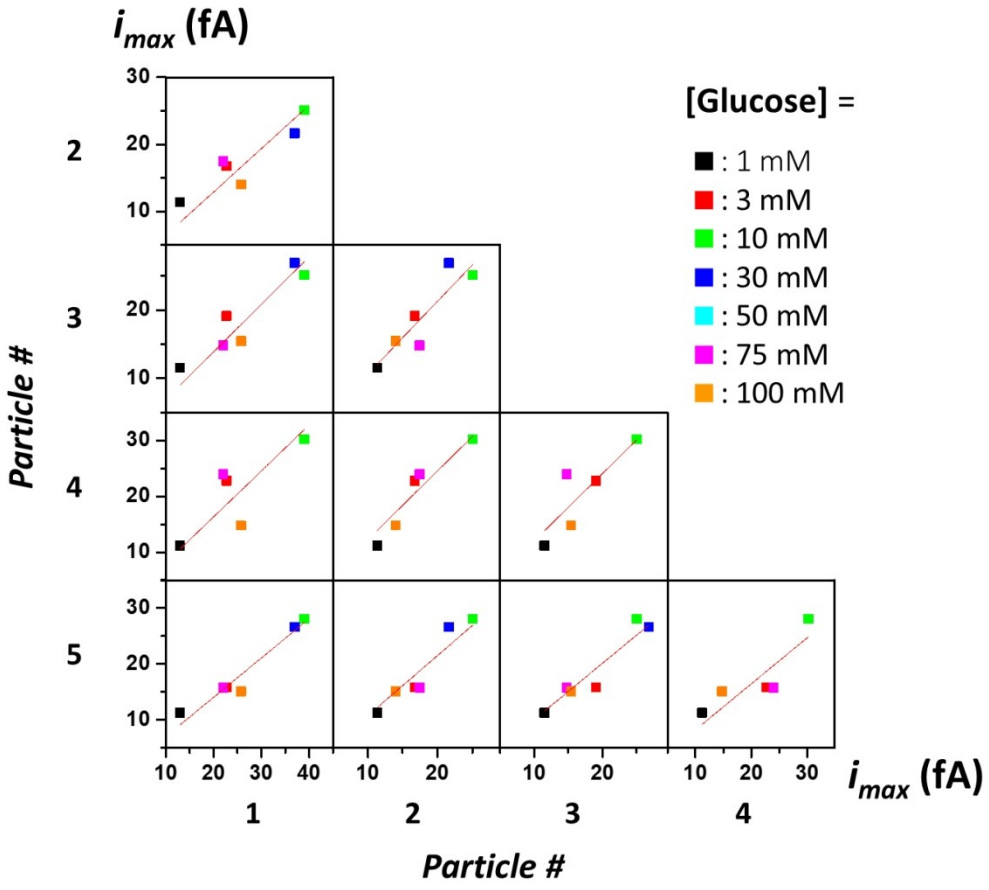

115x103mm (300 x 300 DPI)

View Article Online
DOI: 10.1039/D1NR07445H

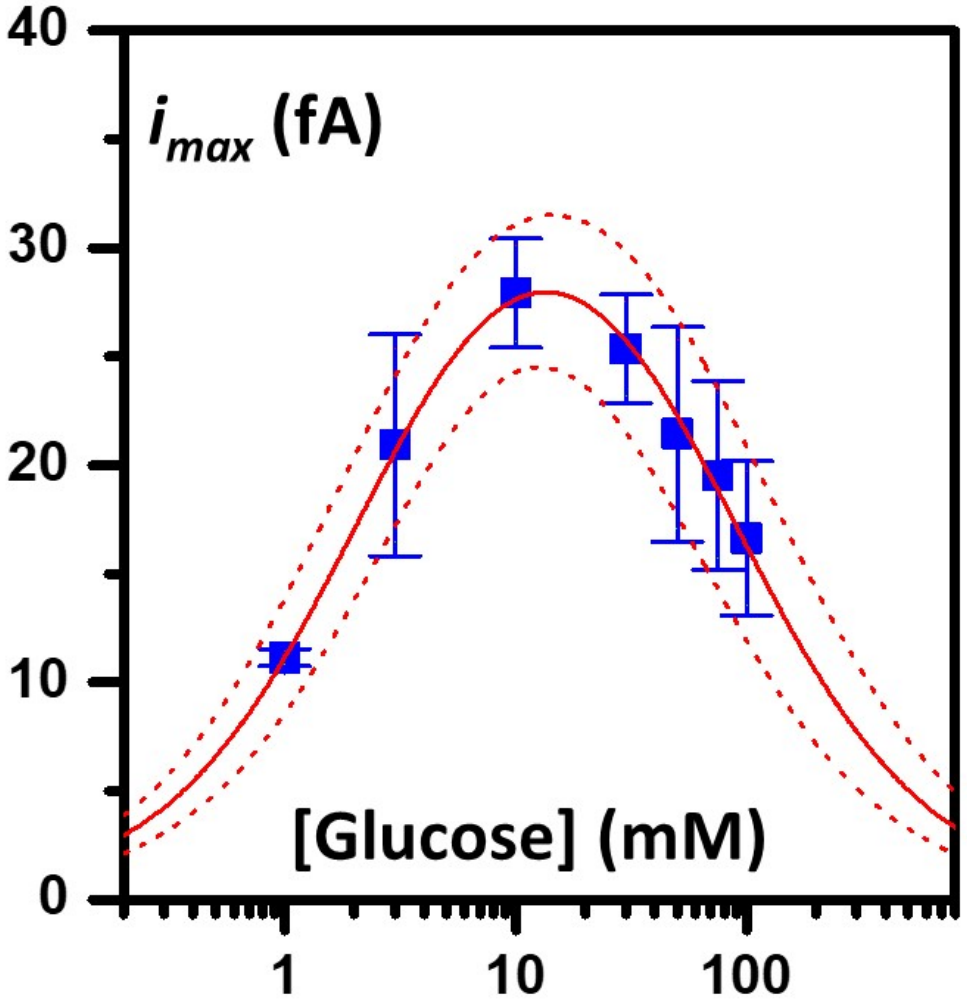

57x61mm (300 x 300 DPI)

View Article Online
DOI: 10.1039/D1NR07445H